Pre-mRNA fate decision safeguards the fidelity of the inflammatory response

Annika Bestehorn[1,2,3], Jeanne Fesselet[1,2,3], Sebastian Didusch[1,2,3], Christina Zeiler[1,2,3], Kevin Doppelmayer[1,2], Martina Borroni[1,2], Anita LeHeron[1,2], Vera Pfanzagl[4], WeiQiang Chen[5], Sara Scinicariello[1,2,3], Manuela Baccarini[1,2], Gijs A Versteeg[1,2], Markus Hartl[5,6], Pavel Kovarik[1,2,*]

[1] Max Perutz Labs, Vienna Biocenter Campus (VBC), Dr.-Bohr-Gasse 9, 1030 Vienna, Austria.
[2] University of Vienna, Center for Molecular Biology, Department of Microbiology, Immunobiology and Genetics, Dr.-Bohr-Gasse 9, 1030 Vienna, Austria.
[3] Vienna BioCenter PhD Program, Doctoral School of the University of Vienna and Medical University of Vienna, Vienna BioCenter (VBC), 1030 Vienna, Austria.
[4] University of Natural Resources and Life Sciences, Vienna, Department of Chemistry, Institute of Biochemistry, Muthgasse 18, 1190 Vienna, Austria
[5] Mass Spectrometry Facility, Max Perutz Laboratories, Vienna Biocenter Campus (VBC), Dr. Bohr-Gasse 7, 1030 Vienna, Austria.
[6] University of Vienna, Center for Molecular Biology, Department for Biochemistry and Cell Biology, Vienna Biocenter Campus (VBC), Dr. Bohr-Gasse 9, 1030 Vienna, Austria
* correspondence pavel.kovarik@univie.ac.at

ABSTRACT

The fidelity of immune responses is dependent on a timely controlled and selective mRNA degradation that is largely driven by RNA-binding proteins (RBPs). It remains unclear whether the selection of an individual mRNA molecule for degradation is governed by stochastic or directed processes. Here, we show that tristetraprolin (TTP, also known as ZFP36), an essential anti-inflammatory RBP, destabilized the target mRNA via a hierarchical molecular assembly. The assembly formation is strictly reliant on TTP interaction with RNA. The TTP homolog ZFP36L1 exhibits similar requirements indicating a broader relevance of this regulatory program. Unexpectedly, the assembly of the cytoplasmic mRNA-destabilization complex is licensed in the nucleus by TTP binding to pre-mRNA while mature cytoplasmic mRNA does not constitute a de novo TTP target. Hence, the fate of an inflammation-induced mRNA is decided concomitantly with its synthesis. This fate decision mechanism prevents the translation of superfluous and potentially harmful inflammation mediators, and ensures an efficient cessation of the immune response irrespective of transcriptional activity.

INTRODUCTION

Functional immune responses are dependent on rapid and precisely controlled adjustments in the transcriptome and proteome to ensure protection against pathogens while minimizing damage to the host. A key safeguarding mechanism against an aggravated immune response is the orchestrated and selective destabilization of mRNAs coding for inflammatory mediators [1]. The major drivers of mRNA destabilization are cis-acting RNA-binding proteins (RBPs) which act mostly as adaptors for the recruitment of the RNA degradation machinery, notably the CCR4-NOT deadenylation and the DCP decapping complexes [2-5]. The selectivity in mRNA destabilization is defined by the interaction of a particular RBP with a sequence or structure in the target RNA molecule. This basic concept of RBP-driven mRNA destabilization is established but elementary questions pertaining to the hierarchy of the process remain unanswered. Consequently, it is unknown whether the fate of an individual mRNA molecule is decided at a defined time and location or whether stochastic events occurring during the mRNA life cycle are the fate drivers. Filling this knowledge gap is required for the understanding of healthy immune responses and for a mechanistic recapitulation of non-resolving inflammation which is often causative of autoimmunity, cancer or neurodegenerative disorders.

To determine the molecular hierarchy of mRNA decay governing the resolution of inflammation we employed TTP which is an mRNA-destabilizing RBP conserved in mammals, with essential functions in the control of inflammatory gene expression [6]. TTP deletion in mice causes a multiorgan inflammation including arthritis, dermatitis, and cachexia, cumulatively known as the TTP deficiency syndrome [7]. The disease develops several weeks after birth on initially healthy mice and progresses to an eventually lethal condition. TTP binds preferentially to adenine-uridine-rich elements (AREs) in 3' untranslated regions (UTRs) via its tandem zinc fingers (TZF) and interacts with both CCR4-NOT and DCP complexes thereby causing destabilization of target mRNAs [8-13]. TTP targets are enriched in but not limited to mRNAs coding for cytokines and chemokines [13-15]. The TTP target spectrum is consistent with the TTP deficiency phenotype which is causatively associated with increased stability and expression of *Tnf*, *Il23*, *Il1a*, *Ccl3*, and possibly other mRNAs [7, 16-18].

RESULTS

RNA binding enables TTP to associate with mRNA degradation complexes and prevents continuous TTP accumulation in the cell nucleus

The cardinal feature of TTP is its ability to orchestrate the timing, extent and selectivity of mRNA decay required for efficient but not exaggerated immune responses. To understand the molecular wiring and the hierarchy of this process we first determined molecular assemblies representing distinct steps of TTP-mediated mRNA decay using APEX2-based proximity-dependent labeling. APEX2 is an engineered ascorbate peroxidase with an improved labeling activity [19]. We fused the murine wild-type TTP (WT; GenBank NP_035886) or an RNA binding-deficient tandem zinc finger TTP mutant (TZF^{mut}) N-terminally to APEX2 to obtain doxycycline-inducible WT-APX and TZF^{mut}-APX expression constructs (**Fig. 1a**). TZF^{mut} was constructed by introducing the mutations C116R and C139R which inactivate the zinc-coordinating properties of each of the two zinc fingers and abolish RNA binding, as reported previously [20]. GFP-APX control was generated to determine the background labeling. The constructs were introduced into HEK293 cells using lentiviral transduction, and their doxycycline (dox)-inducible expression was validated (**Fig. 1b**). To assess a correct signal responsiveness of the TTP fusion proteins, cells expressing the fusion constructs were treated with the stress inducer anisomycin which, similar to other stress cues, increases TTP phosphorylation of S52 and S178 (mouse coordinates) and probably several other residues via the p38 MAPK and MK2 axis [21-23]. Upon anisomycin treatment, a proportion of TTP fusion proteins displayed slower gel mobility, indicative of increased phosphorylation [22] (**Fig. 1b**). Proximity labeling was performed by the addition of biotinphenol for 30 min and subsequent treatment with H_2O_2 for 1 min. Successful labeling in cells expressing WT-APX, TZF^{mut}-APX or GFP-APX was verified by the detection of increased levels of biotinylated proteins in whole-cell-extract samples and streptavidin pull-down samples from H_2O_2-treated cells, as compared to samples from untreated cells (**Extended Data Fig. 1a**). The presence of biotinylated proteins in cells not treated with H_2O_2 results from endogenous biotinylation and biotin-dependent carboxylases [24]. Three replicates of labeled pull-down samples for each of the three constructs (i.e. WT-APX, TZF^{mut}-APX or GFP-WT) were generated. In addition, samples from anisomycin-treated WT-APX- and TZF^{mut}-APX-expressing cells (WT-APX+aniso and TZF^{mut}-APX+aniso) were prepared to estimate the effect of TTP phosphorylation on the proximal interactome. The streptavidin pull-down samples were subject to LC-MS/MS analysis to identify and quantitate biotinylated proteins (**Supplementary Table 1**). The numbers of identified proteins were similar in all sample replicates (**Extended Data Fig. 1b**). Principal component analysis (PCA) of peptide

intensities revealed distinct clusters of the corresponding replicates (**Fig. 1c**). The WT-APX cluster was remarkably well separated from the TZF^{mut}-APX cluster, indicating that binding of TTP to RNA was a major determinant of the TTP interactome. Surprisingly, anisomycin treatment shifted the WT-APX and TZF^{mut}-APX clusters to a unique area in which all anisomycin-treated samples were located. This suggested that stress-induced phosphorylation overruled the differences between the interactomes of wild-type TTP and the RNA binding-deficient mutant.

To identify proteins proximally interacting with TTP we determined the enrichment over the GFP-APX sample for each TTP construct and condition using the amica proteomics data analysis platform [25]. WT-APX displayed 184 enriched proteins while the number of enriched proteins was substantially lower in TZF^{mut}-APX (51 proteins), WT-APX+aniso (37 proteins) and TZF^{mut}-APX+aniso (50 proteins) samples (**Supplementary Table 2** and **Fig. 1d**). The WT-APX interactome comprised the XRN1 exonuclease as well as the deadenylation and decapping components CNOT1, CNOT3, DCP1, DCP2, and EDC3 (**Fig. 1d**) that were previously reported to bind to TTP [9-11, 26, 27]. Strikingly, these proteins were missing in the TZF^{mut}-APX sample suggesting that TTP interacts with the deadenylation and decapping enzymes only following its binding to RNA. The preferential association of CNOT1, DCP1a and EDC3 with WT-APX as compared to TZF^{mut}-APX was verified by Western blotting (**Extended Data Fig. 1c**). The requirement for RNA binding in TTP association with the mRNA processing complexes was unexpected given that previous studies demonstrated specific binding of the subunits of the deadenylation and decapping enzymes to individually expressed N-terminal or C-terminal TTP regions [9-11]. The N-terminal and C-terminal regions were lacking the RNA binding TZF domain which is positioned centrally in the full-length protein. These studies employed in vitro binding assays and overexpression of the binding partners with limited options to address the formation of native protein complexes. Thus, the discrepancy between our data and the findings of previous studies is likely to result from less perturbed conditions and endogenous levels of the deadenylation and decapping complexes in the proximity labeling approach used in our study. Consistent with the reported inhibitory effect of TTP phosphorylation on its binding to deadenylases [28], anisomycin treatment abolished WT-APX interactions with the deadenylase subunits (e.g. CNOT1, CNOT3 – must be consistent with volcano plot) (**Fig. 1d**). Moreover, TTP interactions with the decapping complex were also lost upon anisomycin treatment.

The critical impact of RNA binding and anisomycin treatment on the TTP interactome was further illustrated by the limited overlap of proteins enriched in WT-APX, TZF^{mut}-APX and WT-APX+aniso samples (**Fig. 1e**). Anisomycin changed the divergent WT-APX and TZF^{mut}-APX interactomes into highly similar ones, with WT-APX+aniso and TZF^{mut}-APX+aniso samples

sharing 31 proteins (out 37 and 50, respectively) indicating the acquisition of a uniform proximal environment by RNA-bound and RNA-unbound TTP upon stress (**Extended Data Fig. 1d**).

Top-ranked Gene Ontology (GO) terms significantly overrepresented in the WT-APX interactome, i.e. in proteins enriched in WT-APX over GFP-APX profiles, comprised terms consistent with the established TTP function: GO cellular compartment (CC) included "Cytoplasmic RNP granule" and "P-body", GO biological process (BP) included "posttranscriptional regulation of gene expression" and "mRNA catabolic" process, regulation of RNA stability, and GO molecular function (MF) included "RNA binding" and "mRNA 3' UTR binding" (**Fig. 2a**). In contrast, no such GO terms were found in the TZF^{mut}-APX interactome which instead comprised the terms "Nucleus" and "Nucleoplasm" in the category CC; the categories BP and MF were not informative (**Fig. 2a**). Only few and inconsistent GO terms were overrepresented in the anisomycin-dependent TTP interactomes (WT-APX+aniso and TZF^{mut}-APX+aniso) (**Extended Data Fig. 2a**). Overall, the GO term analysis was conclusive for the WT-APX and TZF^{mut}-APX interactomes: the terms associated with WT-APX allowed inferring the function of TTP in mRNA destabilization while, surprisingly, the terms associated with TZF^{mut}-APX suggested that the RNA binding-deficient TTP localizes in the nucleus (**Fig. 2b**). These conclusions were underpinned by the analysis of the terms "P-body" and "Nucleus" at the gene level showing that the TZF^{mut}-APX interactome was depleted in almost all "P-body" genes while it was enriched in many "Nucleus" genes (**Extended Data Fig. 2b**). Importantly, several "Nucleus" genes were enriched also in the WT-APX interactome (e.g. ATAD5, NFATC1, and MAGEB2) indicating that the WT-APX protein was not excluded from the nucleus (**Extended Data Fig. 2b**), consistent with the predominantly cytoplasmic localization and nucleo-cytoplasmic shuttling of TTP reported previously [22, 29].

The results of proximity labeling experiments were validated by immunofluorescence microscopy using HEK293 cells expressing myc-tagged TTP-WT or TTP-TZF^{mut} proteins. Consistent with the GO term analysis, TTP-TZF^{mut} was confined to the nucleus and TTP-WT localized mostly but not exclusively in the cytoplasm (**Fig. 2c and d**). The difference in the localization pattern was significant (**Extended Data Fig. 2c**). The proximity labeling results were further validated by double immunofluorescence staining showing colocalization of TTP-WT with DCP1a and EDC4 foci (**Fig. 2e and f**), which represent cytoplasmic RNP granules possessing decapping activity [30]. No colocalization of TTP-TZF^{mut} with the DCP1a and EDC4 foci was detected, in agreement with the proximal interactome (**Fig. 2e and f**).

Cumulatively, these results uncover two important functions of RNA binding in the regulation of TTP, i.e. the requirement for RNA binding in maintenance of the cytoplasmic TTP pool and in TTP association with RNA degradation complexes.

Regulation of the interactome and subcellular distribution of TTP by RNA binding is conserved in the TTP protein family and effective also in immune cells

TTP is member of a conserved family of TZF proteins which includes ZFP36L1 and ZFP36L2 [31]. The sequence similarity is the highest in the TZF domain with approximately 70% identity (**Extended Data Fig. 3a**). To test whether the role of RNA binding in the interaction with RNA processing enzymes and in the subcellular localization is conserved in the TTP protein family, we determined the proximal interactomes and subcellular localization of ZFP36L1 and its RNA binding-deficient derivative using the same strategy as for TTP. We generated the APX fusion proteins L1 WT-APX and L1 TZF^{mut}-APX, inducibly expressed them in HEK293 cells and confirmed their labeling activity (**Extended Data Fig. 3b and c**). Following the treatment of L1 WT-APX-, L1 TZF^{mut}-APX- and GFP-APX-expressing cells with biotinphenol and H_2O_2, peptide intensities in streptavidin pull-downs were determined by LC-MS/MS (**Supplementary Table 3**). The replicates of each L1 WT-APX, L1 TZF^{mut}-APX and GFP-APX clustered in separated areas in PCA (**Extended Data Fig. 3d**), similar to TTP samples. Also comparable to the TTP experiments, analysis of proteins enriched in L1 WT-APX or L1 TZF^{mut}-APX samples over GFP-APX revealed a higher number of interaction partners in the L1 WT-APX interactome than in the L1 TZF^{mut}-APX sample (157 versus 17) (**Supplementary Table 4** and **Fig. 3a**). Importantly, proteins found in the L1 WT-APX interactome comprised subunits of the deadenylation and decapping complexes (e.g. CNOT1, CNOT3, EDC3, and DCP1B) while these proteins were missing in the L1 TZF^{mut}-APX interactome (**Fig. 3a**). GO terms overrepresented in proteins enriched in the L1 WT-APX interactome over the L1 TZF^{mut}-APX interactome were consistent with RNA degradation (e.g. “cytoplasmic RNP granule” and “P-body”). These terms were absent from the L1 TZF^{mut}-APX interactome (L1 TZF^{mut}-APX versus L1 WT-APX) which comprised instead terms consistent with nuclear localization (“nuclear lumen” and “nucleus”) (**Fig. 3b**). Immunofluorescence microscopy confirmed L1-TZF^{mut} to localize in the nucleus while the L1-WT protein was predominantly cytoplasmic (**Fig. 3c and d, Extended Data Fig. 3e**). Furthermore, analog to TTP, L1-WT co-localized with DCP1a and EDC4 foci whereas L1-TZF^{mut} did not (**Fig. 3e** and **Extended Data Fig. 3f**). Together, RNA binding enables the association of ZFP36L1 with

the RNA processing complexes and prevents the protein to accumulate in the nucleus indicating that the regulatory function of RNA binding is conserved in the TTP protein family.

The control of inflammatory responses by TTP is best evident in immune cells such as macrophages which abundantly express TTP and the preferred TTP targets including cytokine and chemokine mRNAs [13, 14, 32]. Consequently, to examine the regulation of TTP by RNA binding in a relevant system, we employed the RAW 264.7 murine macrophage cell line. Instead of the APEX2 system we used the TurboID proximity labeling system [33] due to the high level of unspecific APEX2-driven labeling we detected in these cells. We first employed CRISPR/Cas9 to generate RAW 264.7 macrophages deficient in endogenous TTP (hereafter referred to as RAW macrophages) and subsequently introduced in them constructs for inducible expression of TTP or the RNA binding-deficient TTP mutant C-terminally fused to TurboID (TID-WT or TID TZF^{mut}) (**Extended Data Fig. 3g**). The empty TurboID construct (TID-E) was introduced to determine the background labeling. Following mass spectrometry analysis of biotinylated interactomes (**Supplementary Table 5**), PCA of protein intensities showed distinct clusters of TID-WT, TID-TZF^{mut} and TID-E replicates (**Extended Data Fig. 3h**), similar to APEX2-labeled TTP and ZFP36L1 samples in HEK293 cells. GO terms overrepresented in the WT-TID interactome (i.e. TID-WT versus TID-TZF^{mut} comparison, **Supplementary Table 6**) were consistent with RNA degradation (e.g. “cytoplasmic RNP granule” and “P-body”) while such terms were missing in the TID-TZF^{mut} interactome (TID-TZF^{mut} versus TID-WT, **Supplementary Table 6**) (**Fig. 3f**). Instead, the terms overrepresented in the TID-TZF^{mut} interactome were consistent with nuclear localization or nuclear processes. Importantly, one of these terms was also overrepresented in the WT-TID interactome, in agreement with the localization of a minor TTP pool in the nucleus reported previously [22, 29]. These results were similar to those obtained for TTP-APX constructs in HEK293 cells. The consistency of APEX2-dependent TTP interactomes in HEK293 cells and TurboID-dependent TTP interactomes in RAW macrophages were corroborated by GO term analysis of proteins found in the overlap of both approaches: the terms in all three GO categories implied an RNA-destabilizing function of TTP (**Fig. 3g**, **Supplementary Table 7**). Moreover, immunofluorescence microscopy showed TTP-TZF^{mut} to localize in the nucleus while the TTP-WT protein was mostly cytoplasmic (**Fig. 3h, Extended Data Fig. 3i and j**), thereby resembling the localization seen in HEK293 cells.

In summary, the APEX2- and TurboID-based proximity labeling approaches in HEK293 cells and RAW macrophages uncovered a massive impact of RNA binding on the interaction landscape of TTP. The results revealed a hierarchical molecular assembly in which RNA binding is a prerequisite for association of TTP with the RNA degradation machinery. Moreover, RNA

binding-deficient TTP was found to accumulate in the nucleus suggesting that TTP requires RNA binding for its nucleo-cytoplasmic shuttling and the acquisition of the predominantly cytoplasmic localization. The data further showed that the regulatory function of RNA binding is conserved in the TTP protein family.

The primary target of TTP is pre-mRNA not mRNA

The model derived from our proximity labeling and subcellular localization experiments using WT and RNA binding-deficient TTP would predict that the initial contact between TTP and its target RNA occurs in the nucleus and that this complex is subsequently exported to the cytoplasm. This prediction is consistent with previous CLIP-seq experiments carried out in HEK293 cells and macrophages, which univocally proved the ability of TTP to bind to introns in addition to 3' UTRs [13, 14, 34]. We thus hypothesized that the initial TTP target is pre-mRNA rather than mature mRNA. To test this hypothesis, we decided to determine the ratios of pre-mRNA versus mRNA in the TTP-bound RNA pool and compared them to the ratios in the total cellular RNA. If the prediction that TTP primarily targets pre-mRNA was correct, then the pre-mRNA to mRNA ratios should be higher in the TTP-bound RNA pool than in the total cellular RNA (**Fig. 4a**). To isolate TTP-bound full-length RNA molecules we modified the thiouridine (4sU)-facilitated CLIP-seq approach used by us previously [13] in that we omitted the limited RNA hydrolysis step. We expressed myc-tagged TTP in RAW macrophages devoid of endogenous TTP, and induced the expression of TTP targets by stimulation with LPS for 6 h in the presence of 4sU in the last hour of LPS stimulation. Following crosslinking with 365 nm UV, TTP-bound RNA was isolated using pull-down for myc-tagged TTP (P-D samples) and subjected to total RNA-seq, together with the total cellular RNA (input samples), carried out in triplicates. The integrity of input and P-D samples was confirmed by read coverage plots for *Tnf* and *Cxcl2* (**Fig. 4b**) as representatives of TTP targets with nucleotide-resolved binding peaks mapped in a transcriptome-wide study in macrophages (https://ttp-atlas.univie.ac.at/) [13]. The coverage tracks revealed that the pull-downed RNA contained intronic reads indicating the presence of *Tnf* and *Cxcl2* pre-mRNA in P-D samples.

For quantitation of pre-mRNA and mRNA, we separately counted intronic and exonic reads, respectively, as described previously [35], with modifications ensuring read mapping to unambiguous intronic and exonic sequences (see Methods). PCA of normalized intronic and exonic counts in P-D and input showed distinct clusters of corresponding replicates (**Extended Data Fig. 4a**). The means of the three replicates were then calculated for each gene detected in

both, the input and P-D RNA-seq samples (**Supplementary Table 8**), and the mean intronic counts were plotted against the mean exonic counts followed by calculation of linear regression curves (**Fig. 4c**). The regression curve intercept was significantly higher in P-D than in input (-1.7 versus -2.3, respectively) revealing that P-D contained in general higher intronic counts than input (**Fig. 4c**). The regression curve slopes were similar in both P-D and input (0.774 versus 0.778, respectively) showing that the intron enrichment in P-D as compared to input was consistent across the entire spectrum of expressed genes. To determine the enrichment specifically for TTP target genes, we defined TTP target genes based on enrichment in P-D samples (see Methods), and subsequently calculated the intron:exon ratios (In:Ex) in P-D and input for this gene subset (**Supplementary Table 9**). In:Ex ratios calculated for TTP target genes in input samples were in general low (**Extended Data Fig. 4b**), consistent with excess of mRNA over pre-mRNA typical for total cellular RNA. Remarkably, the In:Ex ratios were higher in the P-D sample, pointing to an enrichment of intronic counts in P-D as compared to input (**Extended Data Fig. 4b**). Strikingly, the overall In:Ex ratio was significantly higher in the P-D sample as compared to input (**Fig. 4d**). The difference in the overall In:Ex ratio was well reflected at the level of individual genes as illustrated by the significantly higher In:Ex ratios for *Tnf* and *Cxcl2* in P-D as compared to input (**Fig. 4e**). Given that *Tnf* and *Cxcl2* RNAs are bound by TTP in their 3' UTRs, i.e. in exons not introns (**Fig. 4b**) (https://ttp-atlas.univie.ac.at/) [13], the enrichment in intronic over exonic counts in P-D further corroborates the binding preference of TTP for pre-mRNA rather than mRNA. A similar pre-mRNA enrichment (i.e. In:Ex higher in P-D than in input) was observed for *Il1a* which is a target with a dominant TTP binding peak in the 3' UTR and a distinct TTP site in an intron (**Fig. 4e**) (**Extended Data Fig. 4a**). The In:Ex ratio was high (often close to 1) in targets bound by TTP predominantly in introns as exemplified by *Batf2* which was pulled down essentially as pre-mRNA only (**Fig. 4d**, **Extended Data Fig. 4c**). The pre-mRNA enrichment in P-D seen in RNA-seq data was confirmed by RT-qPCR (**Extended Data Fig. 4d**).

Collectively, the data demonstrate the primary target of TTP is pre-mRNA not mRNA.

Control of inflammation through cytoplasmic mRNA decay is licensed by TTP in the cell nucleus

The preference of TTP to bind pre-mRNA not mRNA raises the possibility that the principal place of TTP binding to a target RNA molecule is the cell nucleus. This would imply that TTP requires nuclear entry for its interaction with the target RNA. To test this possibility, we generated a nuclear import-deficient TTP (nuclear localization signal-mutated TTP, TTP-NLS^{mut}) by introducing the

mutations R126A and R130A (murine TTP coordinates) (**Extended Data Fig. 5a**). These arginine residues were reported to be essential for nuclear import of a TTP TZF peptide [36]. The R126A/ R130A double mutation prevents nuclear import also in the context of the full length TTP since HEK293 cells expressing TTP-NLS^{mut} were devoid of nuclear TTP (**Fig. 5a - c**). In contrast, cells expressing TTP-WT contained a distinct nuclear and a major cytoplasmic TTP pool, as expected (**Fig. 5a - c**). Remarkably, TTP-NLS^{mut} did not co-localize with DCP1A and EDC4 decapping foci (**Fig. 5d - e**). The two arginines mutated in TTP-NLS^{mut} are located in the linker region connecting the two zinc fingers within the TZF domain, i.e. in the central part of TTP (**Fig. 5f**). Given that the interface for the interaction with the decapping complex is located in the N-terminal domain of TTP [26, 27], it is unlikely that the arginine mutations directly impair the interaction of TTP-NLS^{mut} with DCP1A and EDC4. Moreover, the N-terminal domain was shown to autonomously bind to the decapping proteins [26, 27]. Considering the requirement for RNA binding in association of TTP with the decapping complexes (**Fig. 2 and 3**) we reasoned that inability of TTP-NLS^{mut} to associate with DCP1A and EDC4 foci might be caused by an impaired targeting of RNA in cells. To assess whether the R126A/R130A double mutation in TTP-NLS^{mut} directly affected RNA binding, we first examined the structure of the TZF domain. As no structure of full length TTP or the TTP TZF is available, we employed the reported NMR structure of the TZF of the TTP homolog ZFP36L2 in complex with RNA (PDB entry 1RGO) [37]. The TZF domain is conserved in the TTP protein family (**Extended Data Fig. 3a**) and is expected to acquire a similar structure in all TTP protein family members. This expectation was supported by the comparison of the reported NMR structure of the first zinc finger of TTP (PDB entry 1M9O) [38] with the ZFP36L2 TZF (PDB entry 1RGO) (**Extended Data Fig. 5b**). On the grounds of these similarities, we assessed the structural role of the arginine residues that are mutated in TTP-NLS^{mut}, and the potential effects of the R126A/R130A mutations on the zinc fingers and RNA binding. The analysis of conformations of the critical arginines within the respective NMR ensembles of ZFP36L2 TZF and TTP zinc finger 1 structural data revealed a high flexibility of these arginines (**Extended Data Fig. 5b**). Moreover, there is no direct interaction between either of the two relevant arginines and the bound RNA molecule in the ZFP36L2 TZF NMR ensemble (**Fig. 5g**). AlphaFold2 modeling predicted the overall fold of the TTP TZF to be highly similar to that of the ZFP36L2 TZF (**Fig. 5g**), with the critical arginine residues positioned within the conformational space observed in the NMR structures. Consequently, interactions of the two TTP TZF arginines with RNA are unlikely.

To further assess the potential effect of the arginine mutations in TTP-NLS^{mut} on the overall TZF fold we performed structure predictions with AlphaFold2 using CoLabFold, and comparative modelling using the Robetta server. The structural models indicate that the introduction of the

smaller alanine residues, which cannot form hydrogen bonds, may increase the flexibility of the linker region as seen from the increased TTP-NLS^{mut} to ZFP36L2 root-mean-square-deviation (RMSD) compared to that of TTP-WT to ZFP36L2 (**Supplementary Table 10**). However, as the main interaction interfaces of TTP and ZFP36L2 with RNA are the zinc fingers it is unlikely that an increased linker flexibility has a significant impact on the RNA bound state (**Extended Data Fig. 5c**). Collectively, the structural analyses focusing on the TZF domain indicate that the arginine residues R126 and R130 do not contribute to RNA binding, and that the mutation of these residues to alanine does not affect the TZF structural integrity. To address the possible effect of the R126A/R130A double mutation on RNA binding experimentally, we expressed the WT and mutated TZF domains as GST fusion proteins in *E. coli* and used these recombinant proteins (recTZF-WT and recTZF-NLS^{mut}) in RNA EMSA experiments. The results showed that both recTZF-WT and recTZF-NLS^{mut} were able to bind to RNA although the binding of recTZF-NLS^{mut} was weaker when compared to recTZF-WT (**Fig. 5i**). A titration experiment using unlabeled *Tnf* ARE in various ratios to the labeled *Tnf* ARE verified that the labeled *Tnf* ARE was in a similar excess in both, the recTZF-WT and recTZF-NLS^{mut} EMSA experiments (**Extended Data Fig. 5d - e**).

Together, the structural TZF analysis and EMSA experiments using recombinant TZF constructs indicate that the RNA binding site remains functional in TTP-NLS^{mut}. To test whether TTP-NLS^{mut} binds natural target RNAs, i.e. inflammation-associated mRNAs, in immune cells we employed RAW macrophages and the CLIP approach described in **Fig. 4**. We inducibly expressed TTP-WT, TTP-NLS^{mut}, and TTP-TZF^{mut} in RAW macrophages (**Extended Data Fig. 6a**), treated them with LPS and 4sU, and subsequently quantitated the amounts of *Il1a*, *Tnf* and *Il6* mRNAs bound to these TTP constructs in cells. The experiment revealed that the binding of TTP-NLS^{mut} to the target mRNAs in cells was dramatically decreased, resembling the RNA binding-deficient TTP-TZF^{mut} construct (**Fig. 6a**). Consistent with the impairment in mRNA targeting by TTP-NLS^{mut} in cells, the mRNA levels of *Il1a*, *Tnf* and *Il6*, which all code for key pro-inflammatory cytokines, were higher in RAW macrophages expressing TTP-NLS^{mut} as compared to TTP-WT cells (**Fig. 6b**). The deficiency of TTP-NLS^{mut} to control *Il1a*, *Tnf* and *Il6* mRNA levels mimicked the properties of TTP-TZF^{mut} (**Fig. 6b**). These experiments suggest that the deficient association of TTP-NLS^{mut} with the DCP1a and EDC4 foci results from a failure of the nuclear import-deficient TTP mutant to interact with target RNAs in cells despite having a functional RNA binding domain.

Collectively, the results imply that the cytoplasmic TTP pool is impaired in binding to target mRNAs de novo. This finding can be reconciled with the documented degradation of TTP-bound

mRNAs in the cytoplasm [39] if TTP licenses the target by binding to it in the nucleus, i.e. prior to mRNA export to the cytoplasm. Such a nuclear licensing mechanism is in agreement with our data demonstrating preferential binding of TTP to pre-mRNA not mRNA mRNA (**Fig. 4**).

DISCUSSION

Our studies reveal that TTP privileges pre-mRNA over mRNA for binding while cytoplasmic mRNA does not constitute a de novo TTP target. Furthermore, we demonstrate that RNA binding prevents nuclear accumulation of TTP and enables TTP to associate with the cytoplasmic RNA degradation complexes. Importantly, the interaction of TTP with the cytoplasmic RNA degradation complexes is dependent on the ability of TTP to enter the nucleus and engage with the target RNA in this compartment. Collectively, these results are consistent with a model in which TTP binds pre-mRNA in the nucleus and, following maturation of pre-mRNA to mRNA, the TTP-mRNA complex is subsequently exported to the cytoplasm where it associates with the RNA degradation machinery to eliminate the bound RNA and curb inflammation (**Fig. 6c**). Furthermore, our data suggest that the RNA binding-dependent hierarchical model is conserved in the TTP protein family.

Early studies suggested that TTP associates with the decapping and deadenylation enzymes irrespectively of RNA binding and, consequently, that excessive TTP might sequester the RNA degradation complexes from other processes and inhibit mRNA degradation [9-11, 20]. This model was later found inconsistent with the analysis of mice bearing a zinc finger mutation in the TTP locus (C116R knock-in mice) which unequivocally showed that the RNA binding-deficient TTP mutant did not exhibit any dominant-negative effects [40]. Our study provides mechanistic explanations for the results obtained with the C116R knock-in mice in that it excludes the possibility that TTP might seize the decapping and deadenylation enzymes in the RNA-unbound state. Our analyses of the proximal interactomes of TTP and ZFP36L1 indicates that the requirement for RNA binding in the interaction of these proteins with the RNA degradation complexes is likely to be conserved in the entire TTP protein family. This hierarchical assembly of TTP-containing decapping and deadenylation structures is consistent with the current model of the formation of RNP granules, including P- bodies [41]. The model proposes that RNA processing membrane-less granules are hierarchically assembled biomolecular condensates which are dependent upon multi-valent interactions between RNAs and proteins. Proteins with intrinsically disordered regions (IDRs) play an important role the orchestration of the RNP granule formation [42]. Consistently, TTP was recently found to contain an N-terminal IDR which facilitates

the interaction with DCP2 [26]. Another low complexity region is located in the C-terminal part of TTP suggesting that that this region might facilitate other IDR-mediated interactions such as those with the CCR4-CNOT complex which was shown to bind the TTP C-terminal domain [10, 11, 27, 43].

TTP is a largely cytoplasmic protein and exhibits nucleo-cytoplasmic shuttling the significance of which, however, remained unknown [22, 29, 44]. Our study reveals that TTP privileges pre-mRNA over mRNA for binding implicating that the translocation into the nucleus is essential for the interaction of TTP with the natural target RNA. This conclusion is supported by the impaired interaction of a nuclear import-deficient TTP mutant with endogenous target RNAs and, consequently, with the RNA degradation complexes. Together, the data propose that periodic nuclear import and export are indispensable for the TTP life cycle as they continuously couple target binding with target degradation. The predominantly cytoplasmic localization of TTP indicates that the nuclear dwell time of TTP is short. Surprisingly, the appropriate partitioning of TTP into a larger cytoplasmic and smaller nuclear pool is dependent on RNA binding since TTP-TZF^{mut} accumulates in the nucleus. We see this role of RNA binding also in ZFP36L1 suggesting that the regulation of subcellular localization by RNA binding is conserved in the TTP protein family.

The deficiency of TTP-NLS^{mut} to bind TTP targets in cells is intriguing given that structural modeling and assessment of RNA binding by recombinant TZF proteins did not indicate any major perturbances in recTZF-NLS^{mut} as compared to wild type TZF, although we noticed a minor decrease in the RNA binding of the recTZF-NLS^{mut}. The limitation of our structural modeling is the absence of structural data other than the TZF domain. Moreover, TTP is predicted to be unstructured and intrinsically disordered, except for the TZF domain [26]. Hence, the impact of the N-terminal and C-terminal domains on the centrally located TZF domain in cells cannot be currently estimated. Given that N-terminal and C-terminal domains constitute the protein interaction hubs of TTP and are subject to multiple phosphorylations [10, 11, 23, 27, 43, 45], it is feasible that they indirectly regulate the interaction of TTP with RNA in cells. The interaction of TTP with pre-mRNA occurs probably early during the transcription process as evident from the high RNA-seq coverage of full-length pre-mRNAs bound to TTP irrespective of whether the binding sites are in 3' UTRs or introns. The biological significance of TTP binding to intronic regions remains unclear, nevertheless our data suggest that such binding might increase TTP crowding in the nucleus and thereby promote the nuclear dwell time of TTP.

The importance of the precise regulation of immune responses is underlined by the multilayered control of essentially every step of the immune response at the cellular and

organismal level. Our study unravels a nuclear fate decision mechanism ensuring that mRNAs encoding pro-inflammatory mediators are targeted for degradation prior to the pioneering round of translation. This mechanism is driven by binding of TTP to pre-mRNA which, following pre-mRNA processing, licenses the target for subsequent degradation in the cytoplasm. The proposed model minimizes the risks of spurious inflammation-promoting translation that would occur if stochastic processes drove mRNA decay during the immune response.

METHODS

Plasmids

TTP, TTP-TZF point mutant (TTP-TZF^{mut} C116R, C139R) and ZFP36L1 open-reading frame (ORF) were cloned from either modified pcDNA5 FRT TO vector or murine colon total RNA into modified, doxycycline hyclate (dox, Sigma-Aldrich, D9891) inducible lentiviral expression vector pCW 57.1 (Addgene #41393) by Gibson cloning. In brief, C-terminal 3xMyc-tag and backbone complementary overhangs for Gibson assembly were added by PCR. Amplicon was subsequently purified with column DNA Clean-up kit (Monarch PCR & DNA Cleanup Kit, # T1030L, NEB) and mixed with double-digested Nhe1/ BamH1 and gel-purified target pCW57.1 vector in a molecular ratio of 1:2 (50 ng Vector: 12.13 ng Insert). Gibson assembly was performed following the manufacturer's instruction (NEB, E2621S) and transformed into chemically competent DH10B cells. Lentiviral C-terminally 3xMyc-tagged-TTP NLS point mutant (TTP-NLS^{mut}) was generated by mutation of R126 and R130 to alanine. R126A and R130A mutations were inserted into the parental pCW57.1_tetON_TTP-3xMyc vector by site-directed mutagenesis. APEX2 constructs were cloned into a modified pCW57.1 expression vector, gifted to us by Manuela Baccarini. GFP ORF was amplified from pEGFP-N1 (Clontech) by PRC for Gibson cloning. All mentioned dox inducible lentiviral expression vectors (modified pCW57.1) contain a puromycin resistance cassette for selection. N-terminally TurboID TTP (TID-TTP) and empty TurboID (TID-E) vectors were a generous gift from G. Versteeg. They were generated by cloning TID from V5-TurboID-NES_pCDNA3 (Addgene#107169) into a modified pCW57.1 vector (pCW57.1- pCW 57.1-MYC-TurboID-MCS-PGK-mCherry-P2A-rtTA), expressing a constitutively active mCherry selection cassette. TID-TTP-TZF^{mut} was generated by exchanging TTP-WT ORF in parental vector with TTP-TZF^{mut} by conventional restriction digest cloning.

Cell culture and lentiviral transduction

All cell lines in this study were cultured in DMEM (Sigma-Aldrich, D6429) containing 10% FBS and 1% P/S (standard cultivating medium) at 37°C and 5% CO2 in a humified incubator. RAW 264.7 macrophages used in this study bore a CRISPR/Cas9 mediated deletion in the TTP gene. Cells were seeded 24 hours prior to treatments and treatments were directly added to cell culture dishes without exchanging cell cultivating medium. Lentiviral particles were generated by co-transfecting 1.5 µg of total DNA of pMDLg/pRRE (Addgene #12251), pCMV-VSV-G (Addgene #8454), and pRSV-Rev (Addgene #12253) with modified pCW57.1 target vector in a ratio of 5:1:5:5 into HEK293 cells using polyethyleneimine (PEI, Polysciences, 23966) as transfection reagent. Three days post-transfection, viral particles in the supernatant were harvested, passed through a 0.45 µm filter and used to infect either HEK293 cells in a dilution of 1:5 or RAW macrophages in a dilution of 1:2 with 8 µg/ml polybrene (Sigma-Aldrich, TR1003G) containing standard cultivating medium. Successfully transduced cells were selected for by either puromycin (Sigma-Aldrich, P8833-100MG) in standard cultivating medium (3 µg/ml for HEK293 cells or 8 µg/ml for RAW macrophages) for 1 week, or by FACS for mCherry positive cells on day 3 post-infection.

Cell lysates and Western blotting

Expression of TTP-constructs in HEK293 cells and RAW macrophages was induced by 1 µg/µl for 3.5 h (HEK293 cells) or 0.5 µg/ml for 24 h (RAW macrophages). After induction, cells were washed 2x with PBS and lysed in either Frackelton buffer (10 mM Tris-HCl pH8, 30 mM Na4P2O7, 50 mM NaCl, 50 mM NaF, 1% Triton X-100 and 1x cOmplete protease inhibitor cocktail) or RIPA buffer for 5 min on ice. Lysates were cleared by centrifugation at 132000 rpm for 5 min at 4°C and supernatant was transferred into a fresh tube. Protein concentration was determined using Pierce BCA Protein Assay Kit (Thermo-Fisher Scientific, Cat #23225). After concentration adjustment, lysates were mixed at a ratio of 2:1 with SDS loading dye and heated for 5 min at 95°C. Samples were loaded onto 10% SDS polyacrylamide gel for separation, followed by wet transfer onto nitrocellulose membrane (GE Healthcare) in carbonate transfer buffer (3 mM Na_2CO_3, 10 mM $NaHCO_3$, and 20% ethanol) for 16 h at 400 mA and additional 2 h at 200 mA at 4°C. Membranes were blocked in 10% BSA in TBS-T (20 mM Tris, 150 mM NaCl, 0.5% Tween 20, pH 8.0) for 1 h at room temperature (RT) and subsequently incubated with primary antibody overnight at 4°C. The next day, membranes were washed 3x with TBS-T for each 5 min, and incubated with HRP conjugated secondary antibody for 1 h at RT. Chemiluminescence was detected and quantified by using a ChemiDoc Touch Imaging System (BioRad).

Immunofluorescence

$2x10^4$ HEK293 cells, expressing C-terminally 3x Myc-tagged TTP or ZFP36L1 were seeded onto poly-lysine (Sigma-Aldrich, P4832) pretreated glass coverslips for 48 h. TTP or ZFP36L1 expression was induced by dox (1 µg/ml) for 3.5 h. Afterwards, cells were washed 3x with PBS, fixed in 4% formaldehyde in PBS for 10 min at RT and washed again 3x with PBS. Samples were then quenched with 0.1 M Glycine in PBS for 10 min on RT, washed 3x with PBS and subsequently permeabilized with 0.3% Triton in 3% BSA (w/v) in PBS for 30 min on RT. Primary AB (Myc 1:2000, EDC4 1:500, DCP1a 1:500) was diluted in permeabilization solution and incubated for 1 h on RT. After 3x PBS wash, slides were incubated with secondary AB conjugated to either Alexa Fluor 594 (Myc, AF594) or Alexa Fluor 488 (EDC4, DCP1a. AF488) (Thermo-Fisher Scientific, Cat # A-11005, A-11008) for 1 h on RT. Samples were washed 3x with PBS and nuclei were stained with DAPI (0.5 µg/ml, Sigma-Aldrich, D8417-10MG) for 10 min on RT. Then, samples were washed again 2x with PBS and 1x with H_2O and subsequently mounted onto microscopy slides with Prolong Gold antifade reagent (Thermo-Fisher Scientific, P36934). Confocal images were captured on the Zeiss LSM 980 microscope using a 64x oil objective (Plan-Apochromat 1.4NA Oil) with a PMT detector at RT with Zeiss ZEN 3.3 software. All images were analyzed in the Fiji distribution of ImageJ [46]. The mean fluorescence intensity (Mfi) of nuclear TTP was measured by segmenting cells using Otsu thresholding in the DAPI channel to define nuclei boundaries as regions of interest (ROI). The Mfi of ROIs was then measured in the AF594 (Myc) channel. Profile plots were generated with the plot profile function in Fiji by drawing a line through a cell of interest. Data generated by the plot profile function was transferred to Graphpad for generating profile plots, depicting the intensity profiles of respective channels along the line. Colocalization analysis was performed using Comdet v.0.5.5 plug-in in Fiji to detect colocalizing particles in AF594 (Myc) and Alexa Fluor 488 (EDC4, DCP1a) channels. Maximum distance between colocalized spots was set to 4 pixels (~0.28 µm). In AF594 (Myc) channel particles had to reach a size of 7 pixels and an intensity threshold of 50-75, in AF488 channel particles had to reach a size of 10 pixels and an intensity threshold of 100-200.

APEX2 proximity labeling

APEX2 (APX) proximity labeling in HEK293 cells was largely performed as described previously [47] with the following adjustments. Lentivirally-transduced bait protein expression was induced in confluent 15 cm tissue culture-treated dish by 1 µg/ml dox for 3.5 h for TTP-APX MS-experiment. For Zfp36L1-APX MS experiment, bait protein expression was induced by 0.02-1 µg/ml dox for 24h to match protein expression levels. Additionally, indicated samples were treated

with 100 µM anisomycin for 1.5 h within the dox treatment. Labeling substrate biotin phenol was provided to cells for 30 min at an end concentration of 500 µM prior to labeling. Labeling was induced by treating cells for 1 min with 1 mM H_2O_2. Subsequently, cells were quenched by washing 3x with quenching medium (10 mM sodium ascorbate, 5 mM Trolox and 10 mM sodium azide in PBS) and 3x PBS. Labeled cells were lysed in RIPA lysis buffer (50mM Tris HCl pH8, 150mM NaCl, 0.1% SDS, 0.5% sodium deoxycholate, 1% NP-40, 1mM PMSF, 1x cOmplete protease inhibitor cocktail), and protein concentration was measured using Pierce Protein Assay Kit (Thermo-Fisher Scientific, Cat #23225). Prior to affinity purification, streptavidin bead slurry (Thermo-Fisher Scientific, Cat #88817) was acetylated with 5 mM sulfo-NHS acetate in 50 mM ammonium bicarbonate with 0.2% Tween at room temperature for 1 h. In brief, beads were washed 3x with 50 mM HEPES, pH 7.8, 0.2% Tween on a magnetic rack, incubated with sulfo-NHS acetate while rotating for 1 h on RT, subsequently washed in 50 mM ammonium bicarbonate, 0.2% Tween, and finally stored in PBS-T (0.2% Tween), 0.02% sodium azide at 4°C until further usage.1 mg of total protein lysate was loaded onto 150 µl acetylated Streptavidin bead slurry and incubated o/n at 4°C while rotating. The next morning bead samples were washed to remove unspecific binders. Additional washes with 50 mM HEPES pH 7 (5-7x), to remove residual detergents were included prior to mass spectrometry submission. For Western blot analysis, 10% input sample, flow-through samples or eluted samples (P-D) were taken. Elution of P-D was facilitated by heating the bead slurry in 1x SDS loading dye at 95°C for 5 min.

TID proximity labeling

TID proximity labeling in RAW macrophages was performed similarly to APX-based labeling in HEK293 cells with the following differences. Lentivirally transduced RAW macrophages were sorted for similar mCherry signal by FACS and subsequently seeded into 15 cm tissue culture-treated dishes at $7x10^6$ cells, 48 h prior to the experiment. TID-protein expression was induced the next day with 0.025 µg/ml dox (TID-E) or 0.5 µg/ml dox for 24 h to achieve similar expression of the TID constructs. Labeling was performed by supplying cells with 500 µM biotin for 15 min. Afterwards, cells, were washed 3x with PBS and lysed in RIPA lysis buffer (see above). 2 mg of cell lysates were incubated with 100 µl acetylated streptavidin bead slurry o/n at 4°C while rotating. Washing steps and sample preparation for mass spectrometry submission as well as western blot analysis were identical to APX labeling in HEK293 cells.

Sample preparation for mass spectrometry analysis

Beads were transferred to new tubes and resuspended in 50 µl of 50 mM ammonium bicarbonate (ABC). Disulfide bonds were reduced with 10 mM dithiothreitol for 30 min at RT before adding 25 mM iodoacetamide and incubating for another 30 min at RT in the dark. The remaining iodoacetamide was quenched by adding 5 mM DTT and the proteins were digested with 150 ng LysC (mass spectrometry grade, FUJIFILM Wako chemicals) in 1.5 µl 50 mM ammonium bicarbonate at 25°C overnight. The supernatant without beads was incubated with 150 ng trypsin (Trypsin Gold, Promega) in 1.5 µl 50 mM ammonium bicarbonate at 37°C for 5 h. The digest was stopped by the addition of trifluoroacetic acid (TFA) to a final concentration of 0.5 %, and the peptides were desalted using C18 Stagetips [48].

Liquid chromatography-mass spectrometry analysis

Peptides were separated on an Ultimate 3000 RSLC nano-flow chromatography system (Thermo-Fisher Scientific), using a pre-column for sample loading (Acclaim PepMap C18, 2 cm × 0.1 mm, 5 µm, Thermo-Fisher Scientific), and a C18 analytical column (Acclaim PepMap C18, 50 cm × 0.75 mm, 2 µm, Thermo-Fisher Scientific), applying a segmented linear gradient from 2% to 35% and finally 80% solvent B (80 % acetonitrile, 0.1 % formic acid; solvent A 0.1 % formic acid) at a flow rate of 230 nl/min over 120 min.

In TTP-APX labeling experiment, eluting peptides were analyzed on a Q Exactive HF-X Orbitrap mass spectrometer (Thermo-Fisher Scientific), which was coupled to the column with a customized nano-spray EASY-Spray ion source (Thermo-Fisher Scientific) using coated emitter tips (New Objective). The mass spectrometer was operated in data-dependent acquisition mode (DDA), and survey scans were obtained in a mass range of 375-1500 m/z with lock mass activated, at a resolution of 120k at 200 m/z and an AGC target value of 3E6. The 25 most intense ions were selected with an isolation width of 1.4 m/z, isolation offset 0.0 m/z, fragmented in the HCD cell at 28% collision energy and the spectra recorded for max. 100 ms at a target value of 1E5 and a resolution of 30k. Peptides with a charge of +1 or >+6 were excluded from fragmentation, the peptide match feature was set to preferred, the exclude isotope feature was enabled, and selected precursors were dynamically excluded from repeated sampling for 30 seconds.

In L1-APX and TID-TTP labeling experiments, eluting peptides were analyzed on an Exploris 480 Orbitrap mass spectrometer (Thermo-Fisher Scientific) coupled to the column with a FAIMS pro ion-source (Thermo-Fisher Scientific) using coated emitter tips (PepSep, MSWil) with the following settings: The mass spectrometer was operated in DDA mode with two FAIMS

compensation voltages (CV) set to -45 or -60 and 1.5 s cycle time per CV. The survey scans were obtained in a mass range of 350-1500 m/z, at a resolution of 60k at 200 m/z, and a normalized AGC target at 100%. The most intense ions were selected with an isolation width of 1.2 m/z, fragmented in the HCD cell at 28% collision energy, and the spectra recorded for max. 100 ms at a normalized AGC target of 100% and a resolution of 15k. Peptides with a charge of +2 to +6 were included for fragmentation, the peptide match feature was set to preferred, the exclude isotope feature was enabled, and selected precursors were dynamically excluded from repeated sampling for 45 seconds.

MS raw data split for each CV using FreeStyle 1.7 (Thermo-Fisher Scientific), were analyzed using the MaxQuant software package (version 1.6.17.0 for TTP-APX experiment and TID-TTP experiment; version 2.3.1.0 for L1-APX experiment [49] with the Uniprot human reference proteome (version 2020.01 for TTP-APX experiment; version 2022.05 for L1-APX experiment, www.uniprot.org) and mouse reference proteome (version 2020.01, www.uniprot.org), as well as a database of most common contaminants and target protein sequences in TTP-APX experiment and the ZFP36L1_mouse protein sequence in L1-APX experiment. The search was performed with full trypsin specificity and a maximum of two missed cleavages at a protein and peptide spectrum match false discovery rate of 1%. Carbamidomethylation of cysteine residues was set as fixed, oxidation of methionine, and N-terminal acetylation as variable modifications. For label-free quantitation the “match between runs” only within the sample batch and the LFQ function were activated - all other parameters were left at default.

MaxQuant output tables were further processed in R 4.2.1 (https://www.R-project.org) using Cassiopeia_LFQ (https://github.com/moritzmadern/Cassiopeia_LFQ). Reverse database identifications, contaminant proteins, protein groups identified only by a modified peptide, protein groups with less than two quantitative values in one experimental group, and protein groups with less than 2 razor peptides were removed for further analysis. Missing values were replaced by randomly drawing data points from a normal distribution model on the whole dataset (data mean shifted by -1.8 standard deviations, a width of the distribution of 0.3 standard deviations). Differences between groups were statistically evaluated using the LIMMA 3.52.1 [50] at 5% FDR (Benjamini-Hochberg).

Proteomics data analysis

The output from MaxQuant was analyzed with amica software [25]. Proteins from reverse database identifications, potential contaminant proteins and proteins only identified by a modified peptide were removed. Proteins with at least 2 Razor + unique peptides, at least 3 MS/MS counts,

and valid values in 3 replicates in at least one group were considered quantified. LFQ intensities of quantified proteins were log2-transformed and missing values were imputed from a normal distribution downshifted 1.8 standard deviations from the mean with a width of 0.3 standard deviations. Differential expression analysis was performed with DeqMS (version 1.10.0) [51]. In detail, amica was used for principle component analysis, differential analysis of peptide intensities, and over-representation analysis (ORA) using gprofiler2 (version 0.2.1) [52] ($\log_2$ FC > 1 and $p_{adj.} \leq 0.05$). For ORA GO: CC, GO: MF, GO: BP of the gene ontology database [53] were used.

Pull-down of TTP-bound RNA for RNA-Seq and RT-qPCR

Metabolic labeling, crosslinking, harvest and immunoprecipitation of RAW macrophages for qPCR analysis or total RNA seq was performed as described previously [13] with the following alterations: $15x10^6$ Raw macrophages, were seeded into 15 cm tissue culture treated dishes 48 h prior to crosslinking and harvesting. Expression of TTP-Myc constructs was induced with 0.5 µg/µl dox for 24 h in addition to a control omitting dox induction. Cells were stimulated with 10 ng/ml LPS for 6 h to induce endogenous target mRNA expression. 7 h (in qPCR experiment) or 1 h (in RNA-Seq experiment) before harvest, cells were supplied with 100 µM 4sU. TTP-bound RNA was precipitated using 50 µl Pierce™ anti-c-Myc magnetic bead slurry (Thermo-Fisher Scientific, Cat #88843) for 16 h at 4 °C. For the Isotype control, IgG (CST, Cat #5415) bound to Protein A/G magnetic beads (Thermo-Fisher Scientific, Cat # 88802), was included. 10% of total cell lysate per sample was used as total input RNA. After immunoprecipitation, beads were washed in high salt buffer (50 mM Tris-HCl pH 7.4, 1 M NaCl, 1 mM EDTA, 1% NP-40, 0.1% SDS, 0.5% sodium deoxycholate) prior to wash buffer as described [13]. TTP-bound RNA, as well as input RNA, was purified after proteinase K digestion by acidic phenol-chloroform extraction (Ambion) and ethanol precipitation. For quantitation of TTP-bound RNA and total RNA by RT-qPCR with HOT FIREPol EvaGreen qPCR Supermix (Medibena, Cat #SB_08-36-GP) on CFX Touch qPCR cyclers (Bio-Rad), cDNA was produced using random hexamer primers (Mycrosynth) with recombinant M-MuLV reverse transcriptase (RevertAid, Thermo-Fisher Scientific, Cat #K1691). Relative expression levels were calculated with the CFX Maestro Analysis software, as described previously [54]. The following primers were used: 36B4 fw TCCTTCTTCCAGGCTTTGGG and rv GGACACCCTCCAGAAAGCGA; Il1a fw CAAACTGATGAAGCTCGTCA and rv TCTCCTTGAGCGCTCACGAA; pre-Il1a fw GGGACCACTCTCACTAAGCC and rv CTTCCCGTTGCTTGACGTTG; Il6 fw AGTTGCCTTCTTGGGACTGA and rv TTCTGCAAGTGCATCATCGT; Tnf fw

GATCGGTCCCCAAAGGGATG and rv CACTTGGTGGTTTGCTACGAC; pre-Tnf fw GGCAAAGAGGAACTGTAAG and rv CCATAGAACTGATGAGAGG; Irg1 intron fw AACTTTCCAGCCCCACTAGC and rv TAGGAACAGGCCACTGGGTA; Clc2 fw CTTCTGGGCCTGCTGTTCA and rv CCAGCCTACTCATTGGGATCA

RNA-seq

For total RNA-seq, RNA quality was assessed using Agilent RNA 6000 Nano Assays (5067-1511) on an Agilent 2100 Bioanalyzer. RNA sequencing was performed in the VBCF (Vienna BioCenter Core Facilities) Next Generation Sequencing (NGS) Facility (www.viennabiocenter.org/facilities). Library preparation, quality control and sequencing were performed by the NGS facility. Total RNA input samples were subjected to automated ribonucleic depletion using rRNA depletion kit Ribovanish prior to library preparation. Library was prepared using Ultra II Directional RNA Library Prep Kit (NEB, Cat #E7765) for all samples. After library-quality check, samples were sequenced paired end (50 bp) on Illumina NovaSeq S1.

RNA-seq data analysis

Annotations from Genome assembly GRCm39 (02.09.2020) were adapted by filtering for transcripts that were fully expressed at least in one of the sample replicates (defined as having at least one read covering each exon as counted by htseq-count v2.0.4), followed by making intron annotations within the space between two exons of each transcript. Bedtools v2.30.0 subtract and merge were used to first remove sequences with ambiguous (i.e. introns, exons and/or more than one gene) annotations and collapse the remaining annotations to obtain unambiguous annotations for exons and introns for each gene.

Raw RNA-seq reads were adapter- and poly-A trimmed using trim-galore v0.6.10 and poly X and poly G trimmed using fastp v0.23.4, followed by alignment to the reference genome using STAR v2.7.11a. Deduplication and conversion into name-sorted bam files were performed using samtools v1.18. Deeptools' bamCoverage v3.5.2 was used with a bin size of 1 and normalization using counts per million to generate stranded coverage tracks. Htseq-count v2.0.4 was used to count intronic (within intron and intron-exon boundary mapping) and exonic (within exon, exon-exon junction and exon-intron boundary mapping) fragments. Raw exonic and intronic counts were normalized to transcripts per million (TPM) values by normalizing to library size and exon or intron length determined from the collapsed unambiguous genome annotation. Regression analysis was performed comparing the slope and y-intercept for log-log linear models with exonic

normalized counts as predictor and intronic normalized counts as response variable each for input and pull-down using the R functions lm, and car::Anova.

Enrichment analysis was carried out to identify genes more abundant in pull-down than in input. Intronic fragment counts were in general lower than exonic counts, making them more prone to be falsely identified as enriched. To minimize the risk of such false-positives, the threshold for the lowest acceptable counts was defined as average intronic normalized counts in pull-down samples. Genes with normalized intronic or exonic counts (in pull-down) above the threshold were included in the enrichment analysis. Enrichment analysis was performed for intronic and exonic normalized counts separately. Both data sets were first log(ln)-transformed, tested for differences in mean normalized counts of pull-down to input (t-test, two sided) followed by p-value correction using the Benjamini-Hochberg method. Log-fold change was calculated as ln(mean pull-down)-ln(mean input). Significantly enriched genes were defined using the filters $p_{adj.} \leq 0.05$ and log-fold change > 0. In:Ex ratios are means of the quotients of intronic and exonic normalized counts per sample.

Expression of recTZF peptides

BL21(DE3) competent cells were transformed with 50 ng of pGEX-4T-1-GST-TEV.TZF WT/NLS^{mut} expression vector synthesized by Genscript and containing TTP TZF domain (amino acids 93-165, mouse coordinates). As empty control, non-transfected BL21 was used. Over night cultures were diluted with fresh LB medium and grown at 37°C until OD_{600} reached ~0.6. Expression was induced by supplementing cultures with 1 mM ITPG (Sigma), 100 µM $ZnSO_4$ and 0.2% glucose (Sigma, Cat # G8270) for 3 h at 37°C at 165 rpm. Afterwards, cells were harvested by centrifugation and lysed by One shot cell disrupter (Constant Systems Ltd.) with a pressure of 2 kbar in lysis buffer (1 M NaCl, 25 mM HEPES pH 7.4, 0.5 mM PMSF, 1x cOmplete protease inhibitor cocktail). Subsequently, lysates were cleared by centrifugation, 6000 rpm 4°C and protein concentration was estimated by BCA protein assay kits (Thermo-Fisher Scientific, Cat #23225).

RNA Electrophoretic Mobility Shift Assay (RNA EMSA)

RNA EMSA assay was performed using LightShift Chemiluminescent RNA EMSA Kit (Thermo-Fisher Scientific, Cat #20158) according to the manufacturer's instructions. 5' biotinylated and unlabeled *Tnf* ARE probes with the following sequence were purchased from Microsynth: 5'-AUUAUUUAUUAUUUAUUUAUUAUUUA-3'. In brief, HEK293 cells and BL21(DE3) expressing inducible TTP/ TFZ-peptide were harvested as previously described. 15 µg of HEK cell extract and ~100ng of BL21(DE3) extract were incubated with 0.5 µl Poly-U RNA (100 ng/µl, Sigma, Cat#

P9528) 0.25 µl of biotin 5' labeled *Tnf* ARE probe (500 nM), 1x REMSA binding buffer, and 5% Glycerol for 25 min at room temperature. For titration assays, cell lysates were incubated with different ratios of labeled to unlabeled oligo (0x,2x,4x,6x,8x,10x). Subsequently, 1X REMSA Loading Buffer was added and samples were run on a 6% non-reducing polyacrylamide gel for 45 min at 100 V in 0.5x TBE. After wet-blotting in 0.5X TBE for 25 min at 250 mA, the positively charged Nylon membrane was crosslinked by UV light at 120 mJ/cm^2 for 60 s using a commercial UV-light crosslinking instrument equipped with 254 nm bulbs. Biotin signal was detected and quantified by chemiluminescence according to standard LightShift Chemiluminescent RNA EMSA Kit protocol using a ChemiDoc™ Touch Imaging System (BioRad).

TZF structure prediction and modeling

AlphaFold2, USFR ChimeraX and the Robetta server [55-58] were used for structure prediction of TTP TZF defined as region spanning amino acids 93 – 165 (mouse coordinates) corresponding to ZFP36L2 TZF in the PDB entry. Structure prediction using USFR ChimeraX was done without energy minimization. For structure predictions with Robetta comparative modeling PDB entry 1RGO was used as template. Hydrogen bonds were analyzed using UCSF ChimeraX with hydrogen bond parameters set to 0.4 Å distance and 30° angle deviation. root-mean-square-deviation (RMSD) of the models to 1RGO was analyzed by PYMOLalign with cycles set to 0 for all-atom RMSD calculation. Figures were prepared with PYMOL (http://www.pymol.org/).

Quantitation and statistical analysis.

For all experiments, statistical tests, n, and cut-offs are listed in the figure legend. Statistical analysis was performed using GraphPad Prism v.10.0.2 software.

FUNDING

Austrian Science Fund grants W1261, P33000-B and P35852 to PK

Austrian Science Fund grants W1261, P30231-B and P30415-B to GV

Austrian Science Fund grant W1261 to MB

Austrian Science Fund grants SFB F70 and F7007 to MH

ACKNOWLEDGEMENTS

We are grateful to Kevin Eislmayr, Ronja Reinhart, Stefanie Toifl, Josef Laurin and Thomas Peterbauer for fruitful discussions and advice.

REFERENCES

1. Carpenter S, Ricci EP, Mercier BC, Moore MJ, Fitzgerald KA. Post-transcriptional regulation of gene expression in innate immunity. Nature reviews. 2014;14(6):361-76. Epub 2014/05/24. doi: 10.1038/nri3682. PubMed PMID: 24854588.
2. Grudzien-Nogalska E, Kiledjian M. New insights into decapping enzymes and selective mRNA decay. Wiley Interdiscip Rev RNA. 2017;8(1). Epub 2016/07/19. doi: 10.1002/wrna.1379. PubMed PMID: 27425147; PubMed Central PMCID: PMCPMC5179306.
3. Collart MA. The Ccr4-Not complex is a key regulator of eukaryotic gene expression. Wiley Interdiscip Rev RNA. 2016;7(4):438-54. Epub 2016/01/30. doi: 10.1002/wrna.1332. PubMed PMID: 26821858; PubMed Central PMCID: PMCPMC5066686.
4. Turner M, Diaz-Munoz MD. RNA-binding proteins control gene expression and cell fate in the immune system. Nat Immunol. 2018;19(2):120-9. Epub 2018/01/20. doi: 10.1038/s41590-017-0028-4. PubMed PMID: 29348497.
5. Akira S, Maeda K. Control of RNA Stability in Immunity. Annual review of immunology. 2021;39:481-509. Epub 2021/02/13. doi: 10.1146/annurev-immunol-101819-075147. PubMed PMID: 33577347.
6. Blackshear PJ, Perera L. Phylogenetic distribution and evolution of the linked RNA-binding and NOT1-binding domains in the tristetraprolin family of tandem CCCH zinc finger proteins. J Interferon Cytokine Res. 2014;34(4):297-306. Epub 2014/04/05. doi: 10.1089/jir.2013.0150. PubMed PMID: 24697206; PubMed Central PMCID: PMCPMC3976581.
7. Taylor GA, Carballo E, Lee DM, Lai WS, Thompson MJ, Patel DD, Schenkman DI, Gilkeson GS, Broxmeyer HE, Haynes BF, Blackshear PJ. A pathogenetic role for TNF alpha in the syndrome of cachexia, arthritis, and autoimmunity resulting from tristetraprolin (TTP) deficiency. Immunity. 1996;4(5):445-54. Epub 1996/05/01. PubMed PMID: 8630730.
8. Lai WS, Kennington EA, Blackshear PJ. Tristetraprolin and its family members can promote the cell-free deadenylation of AU-rich element-containing mRNAs by poly(A) ribonuclease. Mol Cell Biol. 2003;23(11):3798-812. PubMed PMID: 12748283.
9. Lykke-Andersen J, Wagner E. Recruitment and activation of mRNA decay enzymes by two ARE-mediated decay activation domains in the proteins TTP and BRF-1. Genes Dev. 2005;19(3):351-61. PubMed PMID: 15687258.
10. Sandler H, Kreth J, Timmers HT, Stoecklin G. Not1 mediates recruitment of the deadenylase Caf1 to mRNAs targeted for degradation by tristetraprolin. Nucleic Acids Res. 2011;39(10):4373-86. Epub 2011/02/01. doi: 10.1093/nar/gkr011. PubMed PMID: 21278420; PubMed Central PMCID: PMC3105394.
11. Fabian MR, Frank F, Rouya C, Siddiqui N, Lai WS, Karetnikov A, Blackshear PJ, Nagar B, Sonenberg N. Structural basis for the recruitment of the human CCR4-NOT deadenylase

complex by tristetraprolin. Nat Struct Mol Biol. 2013;20(6):735-9. Epub 2013/05/07. doi: 10.1038/nsmb.2572. PubMed PMID: 23644599.

12. Lai WS, Carballo E, Strum JR, Kennington EA, Phillips RS, Blackshear PJ. Evidence that tristetraprolin binds to AU-rich elements and promotes the deadenylation and destabilization of tumor necrosis factor alpha mRNA. Mol Cell Biol. 1999;19(6):4311-23. Epub 1999/05/18. PubMed PMID: 10330172; PubMed Central PMCID: PMC104391.

13. Sedlyarov V, Fallmann J, Ebner F, Huemer J, Sneezum L, Ivin M, Kreiner K, Tanzer A, Vogl C, Hofacker I, Kovarik P. Tristetraprolin binding site atlas in the macrophage transcriptome reveals a switch for inflammation resolution. Molecular systems biology. 2016;12(5):868. Epub 2016/05/15. doi: 10.15252/msb.20156628. PubMed PMID: 27178967; PubMed Central PMCID: PMC4988506.

14. Tiedje C, Diaz-Munoz MD, Trulley P, Ahlfors H, Laass K, Blackshear PJ, Turner M, Gaestel M. The RNA-binding protein TTP is a global post-transcriptional regulator of feedback control in inflammation. Nucleic Acids Res. 2016;44(15):7418-40. Epub 2016/05/26. doi: 10.1093/nar/gkw474. PubMed PMID: 27220464; PubMed Central PMCID: PMCPMC5009735.

15. Stoecklin G, Tenenbaum SA, Mayo T, Chittur SV, George AD, Baroni TE, Blackshear PJ, Anderson P. Genome-wide analysis identifies interleukin-10 mRNA as target of tristetraprolin. J Biol Chem. 2008;283(17):11689-99. Epub 2008/02/08. doi: 10.1074/jbc.M709657200. PubMed PMID: 18256032; PubMed Central PMCID: PMC2431067.

16. Molle C, Zhang T, Ysebrant de Lendonck L, Gueydan C, Andrianne M, Sherer F, Van Simaeys G, Blackshear PJ, Leo O, Goriely S. Tristetraprolin regulation of interleukin 23 mRNA stability prevents a spontaneous inflammatory disease. J Exp Med. 2013;210(9):1675-84. Epub 2013/08/14. doi: 10.1084/jem.20120707. PubMed PMID: 23940256; PubMed Central PMCID: PMCPMC3754859.

17. Kang JG, Amar MJ, Remaley AT, Kwon J, Blackshear PJ, Wang PY, Hwang PM. Zinc finger protein tristetraprolin interacts with CCL3 mRNA and regulates tissue inflammation. J Immunol. 2011;187(5):2696-701. Epub 2011/07/26. doi: 10.4049/jimmunol.1101149. PubMed PMID: 21784977; PubMed Central PMCID: PMCPMC3159726.

18. Sneezum L, Eislmayr K, Dworak H, Sedlyarov V, Le Heron A, Ebner F, Fischer I, Iwakura Y, Kovarik P. Context-Dependent IL-1 mRNA-Destabilization by TTP Prevents Dysregulation of Immune Homeostasis Under Steady State Conditions. Frontiers in immunology. 2020;11(1398):1398. Epub 2020/08/01. doi: 10.3389/fimmu.2020.01398. PubMed PMID: 32733464; PubMed Central PMCID: PMCPMC7358311.

19. Lam SS, Martell JD, Kamer KJ, Deerinck TJ, Ellisman MH, Mootha VK, Ting AY. Directed evolution of APEX2 for electron microscopy and proximity labeling. Nat Methods. 2015;12(1):51-4. Epub 20141124. doi: 10.1038/nmeth.3179. PubMed PMID: 25419960; PubMed Central PMCID: PMCPMC4296904.

20. Lai WS, Kennington EA, Blackshear PJ. Interactions of CCCH zinc finger proteins with mRNA: non-binding tristetraprolin mutants exert an inhibitory effect on degradation of AU-rich element-containing mRNAs. J Biol Chem. 2002;277(11):9606-13. PubMed PMID: 11782475.

21. Schaljo B, Kratochvill F, Gratz N, Sadzak I, Sauer I, Hammer M, Vogl C, Strobl B, Muller M, Blackshear PJ, Poli V, Lang R, Murray PJ, Kovarik P. Tristetraprolin is required for full anti-inflammatory response of murine macrophages to IL-10. J Immunol. 2009;183(2):1197-206.

Epub 2009/06/23. doi: 10.4049/jimmunol.0803883. PubMed PMID: 19542371; PubMed Central PMCID: PMC2755621.

22. Stoecklin G, Stubbs T, Kedersha N, Wax S, Rigby WF, Blackwell TK, Anderson P. MK2-induced tristetraprolin:14-3-3 complexes prevent stress granule association and ARE-mRNA decay. Embo J. 2004;23(6):1313-24. PubMed PMID: 15014438.

23. Ross EA, Smallie T, Ding Q, O'Neil JD, Cunliffe HE, Tang T, Rosner DR, Klevernic I, Morrice NA, Monaco C, Cunningham AF, Buckley CD, Saklatvala J, Dean JL, Clark AR. Dominant Suppression of Inflammation via Targeted Mutation of the mRNA Destabilizing Protein Tristetraprolin. J Immunol. 2015;195(1):265-76. Epub 2015/05/24. doi: 10.4049/jimmunol.1402826. PubMed PMID: 26002976; PubMed Central PMCID: PMC4472942.

24. Artan M, Hartl M, Chen W, de Bono M. Depletion of endogenously biotinylated carboxylases enhances the sensitivity of TurboID-mediated proximity labeling in Caenorhabditis elegans. J Biol Chem. 2022;298(9):102343. Epub 20220803. doi: 10.1016/j.jbc.2022.102343. PubMed PMID: 35933017; PubMed Central PMCID: PMCPMC9437848.

25. Didusch S, Madern M, Hartl M, Baccarini M. amica: an interactive and user-friendly web-platform for the analysis of proteomics data. BMC genomics. 2022;23(1):817. Epub 20221209. doi: 10.1186/s12864-022-09058-7. PubMed PMID: 36494623; PubMed Central PMCID: PMCPMC9733095.

26. Maciej VD, Mateva N, Schwarz J, Dittmers T, Mallick M, Urlaub H, Chakrabarti S. Intrinsically disordered regions of tristetraprolin and DCP2 directly interact to mediate decay of ARE-mRNA. Nucleic Acids Res. 2022;50(18):10665-79. doi: 10.1093/nar/gkac797. PubMed PMID: 36130271; PubMed Central PMCID: PMCPMC9561381.

27. Fenger-Gron M, Fillman C, Norrild B, Lykke-Andersen J. Multiple processing body factors and the ARE binding protein TTP activate mRNA decapping. Mol Cell. 2005;20(6):905-15. Epub 2005/12/21. doi: 10.1016/j.molcel.2005.10.031. PubMed PMID: 16364915.

28. Clement SL, Scheckel C, Stoecklin G, Lykke-Andersen J. Phosphorylation of tristetraprolin by MK2 impairs AU-rich element mRNA decay by preventing deadenylase recruitment. Mol Cell Biol. 2011;31(2):256-66. Epub 2010/11/17. doi: 10.1128/MCB.00717-10. PubMed PMID: 21078877; PubMed Central PMCID: PMC3019984.

29. Johnson BA, Stehn JR, Yaffe MB, Blackwell TK. Cytoplasmic localization of tristetraprolin involves 14-3-3-dependent and -independent mechanisms. J Biol Chem. 2002;277(20):18029-36. Epub 2002/03/12. doi: 10.1074/jbc.M110465200. PubMed PMID: 11886850.

30. Youn JY, Dunham WH, Hong SJ, Knight JDR, Bashkurov M, Chen GI, Bagci H, Rathod B, MacLeod G, Eng SWM, Angers S, Morris Q, Fabian M, Cote JF, Gingras AC. High-Density Proximity Mapping Reveals the Subcellular Organization of mRNA-Associated Granules and Bodies. Mol Cell. 2018;69(3):517-32 e11. Epub 2018/02/06. doi: 10.1016/j.molcel.2017.12.020. PubMed PMID: 29395067.

31. Wells ML, Perera L, Blackshear PJ. An Ancient Family of RNA-Binding Proteins: Still Important! Trends in biochemical sciences. 2017. Epub 2017/01/18. doi: 10.1016/j.tibs.2016.12.003. PubMed PMID: 28096055.

32. Carballo E, Lai WS, Blackshear PJ. Feedback inhibition of macrophage tumor necrosis factor-alpha production by tristetraprolin. Science. 1998;281(5379):1001-5. Epub 1998/08/14. PubMed PMID: 9703499.

33. Branon TC, Bosch JA, Sanchez AD, Udeshi ND, Svinkina T, Carr SA, Feldman JL, Perrimon N, Ting AY. Efficient proximity labeling in living cells and organisms with TurboID. Nature biotechnology. 2018;36(9):880-7. Epub 20180820. doi: 10.1038/nbt.4201. PubMed PMID: 30125270; PubMed Central PMCID: PMCPMC6126969.

34. Mukherjee N, Jacobs NC, Hafner M, Kennington EA, Nusbaum JD, Tuschl T, Blackshear PJ, Ohler U. Global target mRNA specification and regulation by the RNA-binding protein ZFP36. Genome biology. 2014;15(1):R12. Epub 2014/01/10. doi: 10.1186/gb-2014-15-1-r12. PubMed PMID: 24401661.

35. Madsen JG, Schmidt SF, Larsen BD, Loft A, Nielsen R, Mandrup S. iRNA-seq: computational method for genome-wide assessment of acute transcriptional regulation from total RNA-seq data. Nucleic Acids Res. 2015;43(6):e40. Epub 2015/01/08. doi: 10.1093/nar/gku1365. PubMed PMID: 25564527; PubMed Central PMCID: PMC4381047.

36. Murata T, Yoshino Y, Morita N, Kaneda N. Identification of nuclear import and export signals within the structure of the zinc finger protein TIS11. Biochemical and biophysical research communications. 2002;293(4):1242-7. doi: 10.1016/S0006-291X(02)00363-7. PubMed PMID: 12054509.

37. Hudson BP, Martinez-Yamout MA, Dyson HJ, Wright PE. Recognition of the mRNA AU-rich element by the zinc finger domain of TIS11d. Nat Struct Mol Biol. 2004;11(3):257-64. PubMed PMID: 14981510.

38. Amann BT, Worthington MT, Berg JM. A Cys3His zinc-binding domain from Nup475/tristetraprolin: a novel fold with a disklike structure. Biochemistry. 2003;42(1):217-21. doi: 10.1021/bi026988m. PubMed PMID: 12515557.

39. Stumpo DJ, Lai WS, Blackshear PJ. Inflammation: cytokines and RNA-based regulation. Wiley Interdiscip Rev RNA. 2010;1(1):60-80. Epub 2010/07/01. doi: 10.1002/wrna.1. PubMed PMID: 21956907; PubMed Central PMCID: PMC3915420.

40. Lai WS, Stumpo DJ, Qiu L, Faccio R, Blackshear PJ. A Knock-In Tristetraprolin (TTP) Zinc Finger Point Mutation in Mice: Comparison with Complete TTP Deficiency. Mol Cell Biol. 2018;38(4). Epub 2017/12/06. doi: 10.1128/MCB.00488-17. PubMed PMID: 29203639; PubMed Central PMCID: PMCPMC5789023.

41. Ripin N, Parker R. Formation, function, and pathology of RNP granules. Cell. 2023;186(22):4737-56. doi: 10.1016/j.cell.2023.09.006. PubMed PMID: 37890457; PubMed Central PMCID: PMCPMC10617657.

42. Youn JY, Dyakov BJA, Zhang J, Knight JDR, Vernon RM, Forman-Kay JD, Gingras AC. Properties of Stress Granule and P-Body Proteomes. Mol Cell. 2019;76(2):286-94. doi: 10.1016/j.molcel.2019.09.014. PubMed PMID: 31626750.

43. Lai WS, Stumpo DJ, Wells ML, Gruzdev A, Hicks SN, Nicholson CO, Yang Z, Faccio R, Webster MW, Passmore LA, Blackshear PJ. Importance of the conserved carboxyl-terminal CNOT1 binding domain to tristetraprolin (TTP) activity in vivo. Mol Cell Biol. 2019. Epub 2019/05/01. doi: 10.1128/MCB.00029-19. PubMed PMID: 31036567.

44. Phillips RS, Ramos SB, Blackshear PJ. Members of the tristetraprolin family of tandem CCCH zinc finger proteins exhibit CRM1-dependent nucleocytoplasmic shuttling. J Biol Chem. 2002;277(13):11606-13. Epub 2002/01/18. doi: 10.1074/jbc.M111457200. PubMed PMID: 11796723.

45. Tiedje C, Kotlyarov A, Gaestel M. Molecular mechanisms of phosphorylation-regulated TTP (tristetraprolin) action and screening for further TTP-interacting proteins. Biochemical Society

transactions. 2010;38(6):1632-7. Epub 2010/12/02. doi: 10.1042/BST0381632. PubMed PMID: 21118139.

46. Schindelin J, Arganda-Carreras I, Frise E, Kaynig V, Longair M, Pietzsch T, Preibisch S, Rueden C, Saalfeld S, Schmid B, Tinevez JY, White DJ, Hartenstein V, Eliceiri K, Tomancak P, Cardona A. Fiji: an open-source platform for biological-image analysis. Nat Methods. 2012;9(7):676-82. Epub 20120628. doi: 10.1038/nmeth.2019. PubMed PMID: 22743772; PubMed Central PMCID: PMCPMC3855844.

47. Hung V, Udeshi ND, Lam SS, Loh KH, Cox KJ, Pedram K, Carr SA, Ting AY. Spatially resolved proteomic mapping in living cells with the engineered peroxidase APEX2. Nature protocols. 2016;11(3):456-75. Epub 20160211. doi: 10.1038/nprot.2016.018. PubMed PMID: 26866790; PubMed Central PMCID: PMCPMC4863649.

48. Rappsilber J, Mann M, Ishihama Y. Protocol for micro-purification, enrichment, pre-fractionation and storage of peptides for proteomics using StageTips. Nature protocols. 2007;2(8):1896-906. doi: 10.1038/nprot.2007.261. PubMed PMID: 17703201.

49. Tyanova S, Temu T, Cox J. The MaxQuant computational platform for mass spectrometry-based shotgun proteomics. Nature protocols. 2016;11(12):2301-19. Epub 2016/11/04. doi: 10.1038/nprot.2016.136. PubMed PMID: 27809316.

50. Ritchie ME, Phipson B, Wu D, Hu Y, Law CW, Shi W, Smyth GK. limma powers differential expression analyses for RNA-sequencing and microarray studies. Nucleic Acids Res. 2015;43(7):e47. Epub 2015/01/22. doi: 10.1093/nar/gkv007. PubMed PMID: 25605792; PubMed Central PMCID: PMCPMC4402510.

51. Zhu Y, Orre LM, Zhou Tran Y, Mermelekas G, Johansson HJ, Malyutina A, Anders S, Lehtio J. DEqMS: A Method for Accurate Variance Estimation in Differential Protein Expression Analysis. Mol Cell Proteomics. 2020;19(6):1047-57. Epub 20200323. doi: 10.1074/mcp.TIR119.001646. PubMed PMID: 32205417; PubMed Central PMCID: PMCPMC7261819.

52. Raudvere U, Kolberg L, Kuzmin I, Arak T, Adler P, Peterson H, Vilo J. g:Profiler: a web server for functional enrichment analysis and conversions of gene lists (2019 update). Nucleic Acids Res. 2019;47(W1):W191-W8. doi: 10.1093/nar/gkz369. PubMed PMID: 31066453; PubMed Central PMCID: PMCPMC6602461.

53. Ashburner M, Ball CA, Blake JA, Botstein D, Butler H, Cherry JM, Davis AP, Dolinski K, Dwight SS, Eppig JT, Harris MA, Hill DP, Issel-Tarver L, Kasarskis A, Lewis S, Matese JC, Richardson JE, Ringwald M, Rubin GM, Sherlock G. Gene ontology: tool for the unification of biology. The Gene Ontology Consortium. Nature genetics. 2000;25(1):25-9. doi: 10.1038/75556. PubMed PMID: 10802651; PubMed Central PMCID: PMCPMC3037419.

54. Eislmayr K, Bestehorn A, Morelli L, Borroni M, Walle LV, Lamkanfi M, Kovarik P. Nonredundancy of IL-1alpha and IL-1beta is defined by distinct regulation of tissues orchestrating resistance versus tolerance to infection. Sci Adv. 2022;8(9):eabj7293. Epub 2022/03/03. doi: 10.1126/sciadv.abj7293. PubMed PMID: 35235356; PubMed Central PMCID: PMCPMC8890706.

55. Goddard TD, Huang CC, Meng EC, Pettersen EF, Couch GS, Morris JH, Ferrin TE. UCSF ChimeraX: Meeting modern challenges in visualization and analysis. Protein Sci. 2018;27(1):14-25. Epub 20170906. doi: 10.1002/pro.3235. PubMed PMID: 28710774; PubMed Central PMCID: PMCPMC5734306.

56. Jumper J, Evans R, Pritzel A, Green T, Figurnov M, Ronneberger O, Tunyasuvunakool K, Bates R, Zidek A, Potapenko A, Bridgland A, Meyer C, Kohl SAA, Ballard AJ, Cowie A,

Romera-Paredes B, Nikolov S, Jain R, Adler J, Back T, et al. Highly accurate protein structure prediction with AlphaFold. Nature. 2021;596(7873):583-9. Epub 20210715. doi: 10.1038/s41586-021-03819-2. PubMed PMID: 34265844; PubMed Central PMCID: PMCPMC8371605.

57. Mirdita M, Schutze K, Moriwaki Y, Heo L, Ovchinnikov S, Steinegger M. ColabFold: making protein folding accessible to all. Nat Methods. 2022;19(6):679-82. Epub 20220530. doi: 10.1038/s41592-022-01488-1. PubMed PMID: 35637307; PubMed Central PMCID: PMCPMC9184281.
58. Yang J, Anishchenko I, Park H, Peng Z, Ovchinnikov S, Baker D. Improved protein structure prediction using predicted interresidue orientations. Proc Natl Acad Sci U S A. 2020;117(3):1496-503. Epub 20200102. doi: 10.1073/pnas.1914677117. PubMed PMID: 31896580; PubMed Central PMCID: PMCPMC6983395.
59. Blackshear PJ, Lai WS, Kennington EA, Brewer G, Wilson GM, Guan X, Zhou P. Characteristics of the interaction of a synthetic human tristetraprolin tandem zinc finger peptide with AU-rich element-containing RNA substrates. J Biol Chem. 2003;278(22):19947-55. PubMed PMID: 12639954.

FIGURE LEGENDS

Figure 1. Effects of RNA binding and external stress cues on TTP proximal interactome

a. Schematic representation of constructs used in proximity labeling experiments. Wild-type TTP, RNA binding-deficient tandem zinc finger TTP mutant (TZF^{mut}) and GFP were fused N-terminally to APEX2 downstream of a tetracycline-responsive promoter to obtain WT-APX, TZF^{mut}-APX and GFP-APX constructs. All constructs contained a C-terminal Flag tag. Puromycin was used for cell selection following lentivirus-mediated transduction.

b. Inducible expression of WT-APX, TZF^{mut}-APX and GFP-APX, and effects of stress stimulation. Expression of WT-APX, TZF^{mut}-APX and GFP-APX in HEK293 cells was induced by doxycycline (dox, 1 µg/ml) for 3.5 h. Anisomycin (100 µM, 1.5 h) was used as stress stimulus, as indicated. Subsequently, whole cell lysates were prepared and analyzed by Western blotting using antibodies to APEX (immunoblot, IB: APX) and, as a loading control, vinculin (IB: Vinculin). The position of TTP-APX fusion proteins (WT-APX and TZF^{mut}-APX) and the GFP-APX fusion protein is indicated. Note that anisomycin treatment resulted in the appearance of slower migrating TTP-APX fusions, corresponding to more highly phosphorylated TTP fusion proteins.

c - e. Analysis of APX-based proximal TTP interactome in HEK293 cells by LC-MS/MS. Expression of WT-APX, TZF^{mut}-APX and GFP-APX was induced by doxycycline (dox, 3.5 h). Anisomycin treatment (1.5 h) was employed as indicated (+ aniso). Following labeling with biotinphenol and H_2O_2 biotinylated proteins were enriched by streptavidin pull-down and analyzed

by LC-MS/MS. (**c**) Principal component analysis (PCA) of peptide intensities visualized clustering of biological triplicates and effects of RNA binding (WT-APX vs. TZF^{mut}-APX) and stress stimulation (+ aniso) on the proximal proteome. (**d**) Differential enrichment analysis revealed proteins significantly enriched in WT-APX vs. GFP-APX, TZF^{mut}-APX vs. GFP-APX, WT-APX + aniso vs. GFP-APX, and TZF^{mut}-APX + aniso vs. GFP-APX interactomes. Significantly enriched proteins are depicted in blue ($\log_2$ fold change (FC) > 1, padj. ≤ 0.05, n=3). WT-APX, TZF^{mut}-APX and GFP-APX fusion constructs are underlined. Known TTP interactors DCP1A, DCP2, EDC3, CNOT1, CNOT3 and XRN1 are annotated; bold blue indicates significant enrichment. (**e**) Overlap of proteins enriched in WT-APX, TZF^{mut}-APX, and WT-APX + aniso interactomes.

Figure 2. Regulation of TTP association with mRNA degradation complexes and TTP subcellular localization by RNA binding

a. Overrepresentation of gene ontology (GO) terms in WT-APX and TFZ^{mut}-APX interactomes. Interactomes were defined as proteins significantly enriched over GFP-APX background labeling control ($\log_2$FC ≥ 1 and $p_{adj.}$ < 0.05, n= 3) in LC-MS/MS data. Bar plots depict up to top 10 most significantly overrepresented terms in the GO categories Cellular compartment (CC), Biological process (BP) and Molecular function (MF). Note that the TZF^{mut}-APX interactome did not contain any enriched terms in the MF category and is therefore not shown.

b. Comparison of top eight GO CC terms in the WT-APX interactome and top four GO CC terms in the TZF^{mut}-APX interactome, across all four analyzed interactomes. The CC terms were selected from terms identified in (a). Color coding of the overrepresentation analysis (ORA) values is depicted. Grey color: not significant.

c, d. Immunofluorescence microscopy of C-terminally Myc-tagged TTP-WT and TTP-TZF^{mut} in HEK293 cells. Expression of TTP constructs was induced by doxycycline (1 µg/µl, 3.5 h); control cells were treated with vehicle (DMSO). Constructs were detected with Myc antibody; DAPI visualized the nucleus. (**c**) Immunofluorescence images with profile lines drawn through representative cells (enlarged 2-fold in insets) for quantitation of mean fluorescence intensity (Mfi) in (**d**). Scale bar = 25 µM. (d) Quantitation of Mfi along a profile line drawn through representative cells in (c).

e, f. Colocalization of TTP-WT or TTP-TZF^{mut} with DCP1A and EDC4 foci. TTP-WT and TTP-TZF^{mut} were expressed as in (c). (**e**) Immunofluorescence images showing TTP-WT or TTP-TZF^{mut} and endogenous DCP1A and EDC4. Large images depict TTP constructs visualized by Myc antibody (red); highlighted cells are shown in insets together with DCP1A staining or EDC4 staining (both green) in individual and merged channels. Arrowheads point to foci of DCP1A or

EDC4. Scale bar = 25 µM. (**f**) Quantitation of colocalization of TTP-WT or TTP-TZF^{mut} signals with DCP1A or EDC4 foci using Fiji plugin Comdet (see Methods). Student's t test. **$p_{adj.}$ < 0.01, n = 60 -113 cells

Figure 3. Role of RNA binding in the interactome and subcellular localization within the TTP protein family and in macrophages

a. Analysis of APX-based proximal ZFP36L1 interactome in HEK293 cells by LC-MS/MS. Expression of ZFP36L1 WT-APX (L1 WT-APX), ZFP36L1 TZF^{mut}-APX (L1 TZF^{mut}-APX) and GFP-APX and analysis of biotinylated proteins by LC-MS/MS was carried out as described for TTP constructs in Fig. 2. Differential enrichment analysis revealed proteins significantly enriched in L1 WT (L1 WT-APX vs. GFP-APX) and L1 TZF^{mut}-APX (L1 TZF^{mut}-APX vs. GFP-APX) interactomes. Significantly enriched proteins are depicted in blue ($log_2FC > 1$, p_{adj} j ≤ 0.05, n=3). L1 WT-APX and L1 TZF^{mut}-APX fusion constructs are underlined. Known TTP interactors EDC3, EDC4 and CNOT3 are annotated; bold blue indicates significant enrichment.

b. GO term (CC category) overrepresentation in proteins enriched in L1 WT-APX interactome (L1 WT-APX vs. L1 TZF^{mut}-APX) and in L1 TZF^{mut}-APX interactome (L1 WT-APX vs. L1 TZF^{mut}-APX). Color coding of ORA values is depicted. Grey color: not significant.

c, d. Immunofluorescence microscopy of C-terminally Myc-tagged L1-WT and L1- TZF^{mut} in HEK293 cells. Expression of L1 constructs was induced by doxycycline (1 µg/µl, 3.5 h); control cells were treated with vehicle (DMSO). Constructs were detected with Myc antibody; DAPI visualized the nucleus. (**c**) Immunofluorescence images with profile lines drawn through representative cells (enlarged 2-fold in insets) for quantitation of mean fluorescence intensity (Mfi) in (d). Scale bar = 25 µM. (**d**) Quantitation of Mfi along a profile line drawn through representative cells in (c).

e. Colocalization of L1-WT or L1-TZF^{mut} with DCP1A and EDC4 foci. L1-WT and L1-TZF^{mut} were expressed as in (c). L1 constructs were detected using Myc antibody, endogenous DCP1A and EDC4 were detected using DCP1A and EDC4 antibodies, and colocalization was quantitated using Fiji plugin Comdet (see Methods). Student's t test. **$p_{adj.}$ < 0.01, n= 44-132 cells.

f. GO term overrepresentation in proximal TurboID (TID)-based interactomes of TTP WT (TID-WT) and TTP TZF^{mut} (TID-TZF^{mut}) in RAW macrophages deficient in endogenous TTP (hereafter referred to as RAW macrophages). Expression of TID-WT and TID-TZF^{mut} in RAW macrophages was induced by doxycycline for 24 h followed by biotin labeling for 15 min. Biotinylated proteins were analyzed by LC-MS/MS. GO terms overrepresented in TID-WT and TID-TZF^{mut} interactomes (defined by comparisons TID-WT vs. TID-TZF^{mut} or TID-TZF^{mut} vs. TID-WT, respectively) were

determined using ORA. Top eight GO CC terms in TID-WT and top four GO CC terms in TID-TZF^{mut} are shown. Color coding of ORA values is depicted. Grey color: not significant., and specific TID-WT and TID-TZF^{mut} interactomes were defined as proteins enriched over background labeling by empty TurboID (TID-E).

g. Overlap of TTP interactomes in HEK293 cells (WT-APX vs. GFP-APX) and RAW macrophages (TID-WT vs. TID-E) shown in Venn diagram. Overlap proteins (64 interactors) were subjected to GO term ORA ($\log_2$ FC > 1 and padj. ≤ 0.05).

h. Quantitation of nuclear Mfi of TTP-WT and TTP-TZF^{mut} in RAW macrophages. TTP-WT and TTP-TZF^{mut} expression in RAW macrophages was induced with doxycycline (dox 0.5 µg/ml, 24 h), and localization of TTP constructs was determined by immunofluorescence microscopy using Myc antibody; DAPI was used for nuclear staining. Nuclear masks for quantitation of nuclear Mfi were computationally defined by using ImageJ. Box represents interquartile range, horizontal line in box depicts mean. One-way analysis of variance (ANOVA) with Tukey's multiple comparisons test, n=112, ****$p_{adj.} < 0.0001$.

Figure 4. Quantitation of pre-mRNA and mRNA in TTP-bound RNA molecules in RAW macrophages

a. Design of pull-down (P-D) experiment addressing whether TTP prefers binding to pre-mRNA or mRNA or whether TTP binds randomly to pre-mRNA and mRNA. Following P-D of TTP-bound RNA and subsequent RNA sequencing, the pre-mRNA:mRNA ratio in P-D sample is compared to that in input sample.

b. Coverage plots of RNA-seq analysis of TTP-bound RNA (pull-down samples, P-D) and of total input RNA (input samples) for TTP targets *Tnf* and *Cxcl2*. RAW macrophages bearing an inducible C-terminally Myc-tagged TTP construct were treated with doxycycline (dox 0.5 µg/ml, 24 h) to induce exogenous TTP expression. Subsequently, cells were treated with LPS (10 ng/ml) for 6 h to stimulate expression of TTP targets and with 4sU (100 µM) for 1 h (i.e. 5 h after LPS addition) to metabolically label cellular RNA, and. Following 365 nm crosslinking, cells were lysed and TTP-bound RNA was pulled down (P-D) using Myc beads; 10% of the cell lysate were used for isolation of total cellular RNA (input). P-D and input samples were subjected to RNA-seq and the read coverage for *Tnf* and *Cxcl2* was visualized using Integrative Genomics Viewer (IGV). Shown are representative IGV tracks in input samples, in y axis-zoomed input samples (both in yellow) and in P-D samples (blue). The y axis-zoomed IGV tracks allow visualization of intronic reads, i.e. less abundant reads. The position of previously reported TTP binding peaks [13] is depicted.

c. Visualization of mRNA (exonic counts, x axis) and pre-mRNA (intronic counts, y-axis) in input and P-D samples for all detected genes. Exonic read counts were regarded as mRNA, intronic read counts were regarded as pre-mRNA. Following RNA-seq, read counts of all three replicates were normalized, means for each gene were calculated and the values were plotted (input = yellow, P-D = blue). Linear regression curves revealed significant y-intercept difference between input and P-D samples and no difference in slopes. COvariance (ANCOVA), R function "Anova"-package "car", n=3, ****$p_{adj.} < 0.0001$.

d. Ratios of intronic:exonic (In:Ex) counts for TTP target genes in input and P-D samples. Example TTP target genes are depicted. Difference between In:Ex ratio in input vs. P-D was calculated. Unpaired Student's t test. ***$p_{adj.} < 0.001$**.**

e. In:Ex ratio in input and P-D samples of TTP target genes *Tnf*, *Cxcl2*, *Il1a*, and *Batf2* (means with SD, unpaired Student's t test. **$p_{adj.} < 0.01$, ***$p_{adj.} < 0.001$, ****$p_{adj.} < 0.0001$).

Figure 5. Structure modeling and RNA binding of nuclear import-deficient TTP

a – c. Analysis of subcellular localization of C-terminally Myc-tagged nuclear import-deficient TTP (nuclear localization signal-mutated TTP, TTP-NLS^{mut}) in HEK293 cells by immunofluorescence imaging. Description of the construct see Extended Data Figure 5a. Cells for expression of TTP-NLS^{mut} and TTP-WT were prepared as described in Figure 2c. TTP-NLS^{mut} and TTP-WT expression was induced by doxycycline (1 µg/µl, 3.5 h); control cells were treated with vehicle (DMSO). TTP constructs were detected with Myc antibody; DAPI visualized the nucleus. (**a**) Immunofluorescence images with profile lines drawn through representative cells (enlarged 2-fold in insets) for quantitation of mean fluorescence intensity (Mfi) in (b). Scale bar = 25 µM. (**b**) Quantitation of Mfi along a profile line drawn through representative cells in (a). (**c**) Quantitation of nuclear Mfi of TTP-NLS^{mut} and TTP-WT. Nuclear masks for quantitation of nuclear Mfi were computationally defined by using ImageJ. Box represents interquartile range, horizontal line in box depicts mean. One-way analysis of variance (ANOVA) with Tukey's multiple comparisons test, n=62, ****$p_{adj.} < 0.0001$.

d, e. Colocalization of TTP-WT or TTP-NLS^{mut} with DCP1A and EDC4 foci. TTP-WT and TTP-NLS^{mut} were expressed as in (a). (**d**) Immunofluorescence images showing TTP-WT or TTP-NLS^{mut} and endogenous DCP1A and EDC4. Large images depict TTP constructs visualized by Myc antibody (red); highlighted cells are shown in insets together with DCP1A staining or EDC4 staining (both green) in individual and merged channels. Arrowheads point to foci of DCP1A or EDC4. Scale bar = 25 µM. (**e**) Quantitation of colocalization of TTP-WT or TTP-NLS^{mut} signals

with DCP1A or EDC4 foci using Fiji plugin Comdet (see Methods). Student's t test. **$p_{adj.} < 0.01$, n = 44 -132 cells.

f. Schematic representation of the murine TTP TZF domain used for recombinant protein expression in *E. coli*. TZF domain corresponds to a synthetic peptide previously used in binding studies [59]. Linker region amino acids R126 and R130 mutated in TTP-NLS^{mut} are highlighted in lilac. Zinc finger (ZF) 1 amino acid C116 and ZF2 C139 mutated in TTP-TZF^{mut} are highlighted in blue.

g. Superposition cartoon of NMR structure of ZFP36L2 TZF (black outlines) in complex with RNA (red) (PDB entry 1RGO) and AlphaFold2 model of TTP TZF (blue). ZFP36L2 TZF NMR entry is lacking the most N-terminal and 3 C-terminal amino acids in comparison to TTP TZF selected for recombinant protein studies. R184 (R126 in TTP) and R188 (R130 in TTP) are shown as balls & sticks (yellow) and highlighted in rectangles. Zinc ions are shown as grey spheres. Residues in ZFP36L2 involved in π- π staking with RNA are shown in blue and residues involved in hydrogen bonds are depicted in green.

h, i. Binding of recombinant TZF-WT and TZF-NLS^{mut} GST fusion proteins (recTZF-WT and recTZF-NLS^{mut}) to *Tnf* ARE assessed by RNA EMSA. (**h**) recTZF-WT and recTZF-NLS^{mut} were expressed in *E. coli* and cleared lysates were used for chemiluminescence-based RNA EMSA. Lysates from *E. coli* without recombinant TZF constructs were used as control (Empty). Representative RNA EMSA of 5 independent experiments is shown. (**i**) Quantitation of RNA EMSA shown in (h). Images were acquired and quantitated using ChemiDoc (BioRad). *Tnf*-ARE-bound fraction was determined as ratio of bound versus total *Tnf*-ARE. ANOVA, means with SDs, non-significant (ns), n=5.

j. Western blot showing expression of recTZF-WT and recTZF-NLS^{mut} in *E. coli* lysates used in (h). recTZF-WT and recTZF-NLS^{mut} was detected by immunoblotting with GST antibody (IB: GST).

Figure 6. Analysis of de novo binding of TTP to mature cytoplasmic mRNAs representing natural TTP targets in immunostimulated RAW macrophages

a. Analysis of mRNAs bound to TTP (TTP-WT) or to constitutively cytoplasmic TTP (TTP-NLS^{mut}). TTP-WT and TTP-NLS^{mut} were inducibly expressed in RAW macrophages as described in Figure 3h. TTP-TZF^{mut} was included as negative control. Cells were treated with LPS and 4sU as described n Extended Data Figure 4d. Following 365 nm crosslinking, cells were lysed and TTP-bound RNA was pulled down using Myc beads; 10% of the cell lysate were used for isolation of total cellular RNA (input). Control analyses were carried out using mouse IgG isotype antibody

instead of Myc antibody, and using RAW macrophages treated with vehicle (DMSO) instead of the TTP expression-inducing doxycycline. Enrichment of *Il1a, Tnf* and *Il6* mRNA in pull-down fraction from TTP-WT, TTP-NLS^{mut}, and TTP-TZF^{mut} RAW macrophages is depicted and shown as fold difference between pull-down and input. *36b4* mRNA was used and non-TTP target control. One-way analysis of variance (ANOVA), means of RT-qPCR data with SDs, n = 3 (each in triplicates), ***$p_{adj.} < 0.001$, ****$p_{adj.} < 0.0001$.

b. Levels of *Il1a, Tnf* and *Il6* mRNA in RAW macrophages inducibly expressing TTP-WT, TTP-NLS^{mut}, and TTP-TZF^{mut} constructs. Expression of TTP constructs was induced with doxycycline (dox 0.5 µg/ml, 24 h) followed by LPS stimulation (10 ng/ml, 6 h). Note that RAW macrophages were devoid of endogenous TTP similar to other experiments in this study. Expression of the housekeeping gene *36b4* was used for normalization. Data are presented as means and SDs, with all data points shown. ANOVA n = 3, each measured in triplicates, ***$p_{adj.} < 0.001$, ****$p_{adj.} < 0.0001$.

c. Model of mRNA degradation by a TTP binding & nucleo-cytoplasmic shuttling cycle. The model proposes that, following TTP translation or release upon degradation of bound mRNA, TTP translocates to the nucleus (Step 1), to bind pre-mRNA (Step 2). Subsequently, pre-mRNA is processed to mRNA, and the TTP-mRNA complex is exported to the cytoplasm (Step 3) where it associates with RNA degradation machinery to eliminate the bound RNA (Step 4).

EXTENDED DATA FIGURE LEGENDS

Extended Data Figure 1 (relates to Figure 1). Proximity labeling quality control and validation

a. Biotinylation activity of APX constructs analyzed by Western blotting. WT-APX, TZF^{mut}-APX and GFP-APX expression in HEK293 cells was induced (dox, 3.5 h) followed by the addition of biotinphenol and H_2O_2. H_2O_2 was omitted, as indicated, to assess endogenous biotinylation. Cell lysates (Input) were subjected to streptavidin pull-down to enrich labeled proteins; pull-down efficiency was estimated by the flow-through analysis. Immunoblotting using biotin antibodies (IB: Biotin) revealed biotinylated proteins. The overall higher biotin signal in H_2O_2-treated Input and F-T samples indicates APX-dependent labeling; the biotin signal in samples without H_2O_2 treatment indicates endogenous biotinylation.

b. Number of proteins identified in individual replicates by LC-MS/MS. The number of identified proteins in each replicate is calculated from the LFQ intensities before imputation, and reflects peptides mapped to the protein database.

c. Validation of LC-MS/MS-detected interactions by Western blotting. WT-APX, TZF^{mut}-APX and GFP-APX expression in HEK293 cells was induced (dox, 3.5 h) followed by the addition of biotinphenol and H_2O_2. H_2O_2 was omitted as indicated to obtain background signals. Cell lysates (Input), streptavidin pull-down and flow-through samples were analyzed by immunoblotting using antibodies to APX, CNOT1, DCP1A and EDC3. Note that immunoblotting for EDC3 was carried out following immunoblotting using APX antibodies so that the signal above the EDC3 band results from incomplete stripping of APX antibodies from the membrane.

d. Overlap of proteins enriched in WT-APX+aniso (WT-APX+aniso vs. GFP-APX) and TZF^{mut}-APX+aniso (TZF^{mut}-APX+aniso vs. GFP-APX) interactomes. $\log_2$ fold change (FC) > 1, padj. ≤ 0.05, n=3

Extended Data Figure 2 (relates to Figure 2). GO term analysis of TTP interactome upon stress, gene-level analysis of representative TTP interactomes, and quantitation of effects of RNA binding on nuclear localization of TTP

a. Overrepresentation of GO terms in WT-APX + aniso. and TFZ^{mut}-APX + aniso. interactomes. Interactomes were defined as proteins significantly enriched over GFP-APX background labeling control ($\log_2$FC ≥ 1 and $p_{adj.}$ < 0.05, n= 3) in LC-MS/MS data. Bar plots depict significantly overrepresented terms in the GO categories CC, BP and MF. Note that the TZF^{mut}-APX + aniso. interactome did not contain any enriched terms in the MF category and is therefore not shown.

b. Proteins from GO terms P-body (GO:000932) and Nucleus (GO: 0005634) found enriched in WT-APX or TZF^{mut}-APX interactomes. Black circles: significantly enriched proteins; blue circles: proteins not enriched. Fold-change (Log_2FC) enrichment is indicated by color code.

c. Quantitation of nuclear Mfi of TTP-WT and TTP-TZF^{mut}. Nuclear masks for quantitation of nuclear Mfi were computationally defined by using ImageJ. Box represents interquartile range, horizontal line in box depicts mean. One-way analysis of variance (ANOVA) with Tukey's multiple comparisons test, n=62, ****$p_{adj.}$ < 0.0001.

Extended Data Figure 3 (relates to Figure 3). Dependence of interactomes and subcellular localization of ZFP36L1 in HEK293 cells and of TTP in RAW macrophages on RNA binding

a. Multiple sequence alignment of TZFs of murine TTP (NP_035886), ZFP36L1 (NP_031590) and ZFP36L2 (NP_001001806). TZF is defined as a 73 amino acid long region comprising zinc fingers (ZFs) 1 and 2, linker between ZFs, conserved N-terminal leader sequence and seven amino C-terminal amino acids, as reported [59]. ZF cysteines and histidines are highlighted in blue; arginines important for the nuclear localization are in lilac.

b. Schematic representation of ZFP36L1 WT and TZF^{mut} fused N-terminally to APEX2 (L1 WT-APX and L1 TZF^{mut}-APX) downstream of a tetracycline-responsive promoter. All constructs contained a C-terminal Flag tag. Puromycin was used for cell selection following lentivirus-mediated transduction of HEK293 cells.

c. Biotinylation activity of ZFP36L1 APX constructs analyzed by Western blotting. L1 WT-APX, L1 TZF^{mut}-APX, and GFP-APX expression in HEK293 cells was induced (0.5 µg/ml dox, 16 h) followed by the addition of biotinphenol and H_2O_2. Controls without dox treatment were included. Cell lysates (Input) were subjected to streptavidin pull-down (P-D) to enrich labeled proteins; pull-down efficiency was estimated by the flow-through (F-T) analysis. Immunoblotting using biotin antibodies (IB: Biotin) revealed biotinylated proteins. The biotin signal in samples without dox indicates endogenous biotinylation.

d. PCA of peptide intensities visualizing clustering of biological triplicates of L1 WT-APX, L1 TZF^{mut}-APX and GFP-APX.

e. Quantitation of nuclear Mfi of L1-WT and L1 TZF^{mut}. L1-WT and L1-TZF^{mut} expression in HEK293 cells was induced and localization was determined as described in Figure 3c. Nuclear masks for quantitation of nuclear Mfi were computationally defined by using ImageJ. Box represents interquartile range, horizontal line in box depicts mean. One-way analysis of variance (ANOVA) with Tukey's multiple comparisons test, n=44, ***$p_{adj.} < 0.001$, ****$p_{adj.} < 0.0001$.

f. Colocalization of L1-WT or L1-TZF^{mut} with DCP1A and EDC4 foci. L1-WT and L2-TZF^{mut} were expressed as in Figure 3c. Immunofluorescence images show L1-WT or L1-TZF^{mut} and endogenous DCP1A and EDC4. Large images depict L1 constructs visualized by Myc antibody (red); highlighted cells are shown in insets together with DCP1A staining or EDC4 staining (both green) in individual and merged channels. Arrowheads point to colocalized foci of DCP1A or EDC4 with TTP. Scale bar = 25 µM.

g. Schematic representation of TTP WT and TTP TZF^{mut} C-terminally fused to TurboID (TID-WT and TID-TZF^{mut}) and allowing doxycycline-inducible expression in RAW macrophages. TID-empty (TID-E) was included as a background labeling control. All constructs were N-terminally Myc tagged. Puromycin resistance served for selection following lentiviral transduction of RAW macrophages.

h. PCA of peptide intensities visualizing clustering of four biological replicates of TID-WT, TID-TZF^{mut} and TID-E.

i, j. Subcellular localization of TTP-WT and TTP-TZF^{mut} in RAW macrophages. TTP-WT and TTP-TZF^{mut} expression was induced as in Figure 3h; DMSO was used as vehicle control. (**i**) Immunofluorescence images visualize TTP-WT and TTP-TZF^{mut} detected using Myc antibody

(red); DAPI was used for nuclear staining (blue). Profile lines was drawn through representative cells for Mfi quantitation. (**j**) Quantitation of nuclear Mfi of TTP-WT and TTP-TZF^{mut} in RAW macrophages. Nuclear masks for quantitation of nuclear Mfi were computationally defined by using ImageJ. Box represents interquartile range, horizontal line in box depicts mean. One-way analysis of variance (ANOVA) with Tukey's multiple comparisons test, n=112, ****$p_{adj.} < 0.0001$.

Extended Data Figure 4 (relates to Figure 4). Differential enrichment of pre-mRNA versus mRNA in TTP-bound RNA in RAW macrophages

a. Intronic and exonic RNA-seq read counts of TTP-bound RNA (pull-down, P-D) and of total input RNA (input) analyzed by PCA. RAW macrophage treatment and RNA isolation were carried out as described in Figure 4b. Following read mapping, exonic and intronic reads were annotated and separately counted. Replicates of individual samples are depicted as indicated.

b. TTP target gene distribution according to intronic to exonic RNA-seq read count ratios (In:Ex) in P-D and input samples. Histogram of RNA-seq data for TTP targets shows generally lower In:Ex ratios in input than in P-D. are derived from The histogram reveals mber of individual transcripts detected in both Input and PD samples with a distinct In/ex ratio and their distribution within input and P-D samples.

c. Representative IGV tracks for TTP targets *Il1a* and *Batf2* in input and P-D samples. Data generation and visualization as described in Figure 4.

d. Analysis of TTP-bound pre-mRNAs by RT-qPCR. Cells were prepared as described in Figure 4b. Cells were treated with 4sU (100 μM) for 7 h to metabolically label cellular RNA, and with LPS (10 ng/ml) for 6 h (i.e. 1 h after 4sU addition) to stimulate expression of TTP targets. Pull-down RNA and input RNA were generated as described in Figure 4b, and subjected to pre-mRNA-specific RT-qPCR analysis. Control analyses were carried out using mouse IgG isotype antibody instead of Myc antibody, and using RAW macrophages treated with vehicle (DMSO) instead of the TTP expression-inducing doxycycline. Pre-mRNA enrichment in TTP-bound RNA shown as fold difference between pull-down and input. One-way analysis of variance (ANOVA), means of RT-qPCR data with SDs, n = 3, each measured in triplicates, ***$p_{adj.} < 0.001$, ****$p_{adj.} < 0.0001$.

Extended Data Figure 5 (relates to Figure 5). Structure modeling and RNA binding of TTP TZF and nuclear import-deficient TTP mutant TZF-NLS^{mut}

a. Schematic representation of nuclear import-deficient C-terminally Myc-tagged TTP-NLS^{mut} for doxycycline-inducible expression.

b. NMR ensemble conformations of arginine residues critical for functional NLS in and TTP. Reported NMR structure of RNA-bound ZFP36L2 TZF (PDB: 1RGO) and all conformations (20 states in NMR ensemble) of R184 and R188 (full length coordinates) shown on left. Reported NMR structure of TTP ZF1 (PDB: 1M9O) and all conformations (23 states in NMR ensemble) of R126 (full length coordinate) shown on right. Only R126 is comprised in the available TTP ZF1 structure. Relevant R amino acids shown as balls and sticks, protein backbone structures shown as cartoon.

c. Superposition of TTP TZF-WT (left, blue) and TTP TZF-NLS^{mut} (right, pink) AlphaFold2 models with NMR structure of ZFP36L2 TZF (1RGO, state 11, black outline). Protein backbones shown as cartoons, relevant R residues shown as balls & sticks and highlighted in rectangles, zinc ions shown as grey spheres. Mutations of R into A in TTP TZF-NLS^{mut} (right, lilac) are highlighted in rectangles and visible against R residues in ZFP36L2 background (black outline).

d, e. Binding of recombinant TZF-WT and TZF-NLS^{mut} GST fusion proteins (recTZF-WT and recTZF-NLS^{mut}) to *Tnf* ARE assessed by RNA EMSA upon different excess of unlabeled *Tnf*-ARE. (**d**) RNA EMSA was performed as described in Figure 5h except for the presence of 0x, 1x, 2x, 4x, 6x, 8x or 10x excess of unlabeled *Tnf*-ARE. Images are representative of three independent experiments. (**e**) Quantitation of RNA EMSA shown in (d). Images were acquired and quantitated using ChemiDoc (BioRad). *Tnf*-ARE-bound fraction was determined as ratio of bound versus total labeled *Tnf*-ARE and depicted as means and SDs (n=3), in $\log_{10}$ scale.

Extended Data Figure 6 (relates to Figure 6). Expression analysis of TTP-WT, TTP-NLS^{mut}, and TTP-TZF^{mut} RAW macrophages

Western blot showing protein levels of TTP-WT, TTP-NLS^{mut} and TTP-TZF^{mut} in RAW macrophage cells lysates (Input) and Myc antibody pull-down fractions used Figure 6a. Control samples include mouse IgG isotype antibody instead of Myc antibody, and using RAW macrophages treated with vehicle (DMSO) instead of the TTP expression-inducing doxycycline. TTP constructs were detected by immunoblotting with TTP antibodies (IB: TTP).

SUPPLEMENTARY TABLE CAPTIONS

Table S1. LFQ (label-free quantitation) intensity and total spectral counts of all proteins identified in WT-APX, TZF^{mut}-APX, WT-APX+aniso, TZF^{mut}-APX+aniso and GFP-APX samples.

Table S2. Proteins identified as significantly enriched ($log_2FC \geq 1$ and $p_{adj.} < 0.05$ over GFP-APX, n= 3) in comparisons of WT-APX vs. GFP-APX, TZF^{mut}-APX vs. GFP-APX, WT-APX+aniso vs. GFP-APX, and TZF^{mut}-APX+aniso vs. GFP-APX proximity labeling interactomes.

Table S3. LFQ (label-free quantitation) intensity and total spectral counts of all proteins identified in L1 WT-APX, L1 TZF^{mut}-APX and GFP-APX samples.

Table S4. Proteins significantly enriched ($log_2FC \geq 1$ and $p_{adj.} < 0.05$, n= 3) in comparisons of L1 WT-APX vs. GFP-APX, L1 TZF^{mut}-APX vs. GFP-APX, L1 WT-APX vs. L1 TZF^{mut}-APX, and L1 TZF^{mut}-APX vs. L1 WT-APX interactomes.

Table S5 LFQ intensity and total spectral counts of all proteins identified in TID-WT, TID-TZF^{mut}, and TID-E samples.

Tables S6. Proteins significantly enriched ($log_2FC \geq 1$ and $p_{adj.} < 0.05$, n= 3) in comparisons of TID-TTP variants and TID-E background labeling control identified by TID-based proximity labeling RAW macrophages.

Table S7. Overlap of TTP interactomes in HEK293 cells and RAW macrophages. TTP interactome in HEK293 cells is defined as proteins enriched ($log_2FC \geq 1$ and $p_{adj.} < 0.05$, n= 3) in WT-APX vs. GFP-APX comparison (Table S2). TTP interactome in RAW macrophages is defined as proteins enriched ($log_2FC \geq 1$ and $p_{adj.} < 0.05$, n= 3) in TID-WT vs. TID-E comparison (Table S6).

Table S8. Table reports ENSEMBL IDs, TPM normalized counts based on counting reads with unambiguous intron and exon annotations, mean count value, and gene symbols for the genes that were identified in both P-D and input samples. Normalized counts were calculated from raw counts by normalizing first to library size per 1 million fragments and subsequently to exon or intron length (unambiguous, collapsed) per 1 kb for each gene.

Table S9. Table lists TTP target genes identified as genes with enriched counts in P-D vs. input samples. logFC and p_adj. value. Threshold for the inclusion of genes in the analysis of either

intronic or exonic count enrichment was set to the mean of intronic normalized counts in the pull-down sample (3.891038).

Table S10. AlphaFold2 and Robetta data.

Figure 1

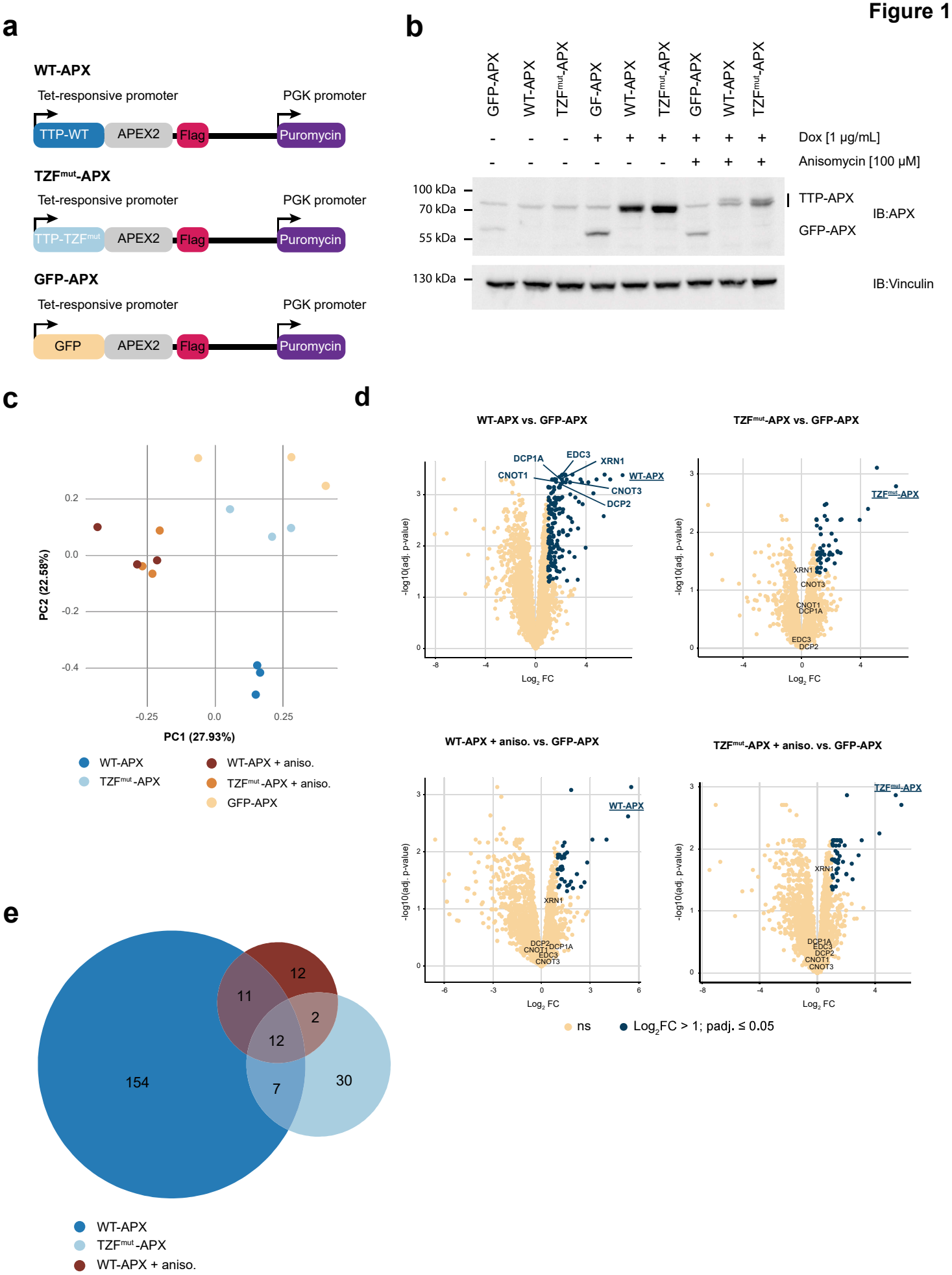
a
WT-APX
Tet-responsive promoter
PGK promoter
TTP-WT
APEX2
Flag
Puromycin
TZFmut-APX
TTP-TZFmut
GFP-APX
GFP
b
GFP-APX
WT-APX
TZFmut-APX
GF-APX
Dox [1 µg/mL]
Anisomycin [100 µM]
100 kDa
70 kDa
55 kDa
130 kDa
TTP-APX
GFP-APX
IB:APX
IB:Vinculin
c
PC2 (22.58%)
PC1 (27.93%)
WT-APX
TZFmut-APX
WT-APX + aniso.
TZFmut-APX + aniso.
GFP-APX
d
WT-APX vs. GFP-APX
TZFmut-APX vs. GFP-APX
WT-APX + aniso. vs. GFP-APX
TZFmut-APX + aniso. vs. GFP-APX
-log10(adj. p-value)
Log2 FC
DCP1A
EDC3
XRN1
CNOT1
CNOT3
DCP2
WT-APX
TZFmut-APX
ns
Log2FC > 1; padj. ≤ 0.05
e
154
11
12
2
12
7
30
WT-APX
TZFmut-APX
WT-APX + aniso.

Figure 2

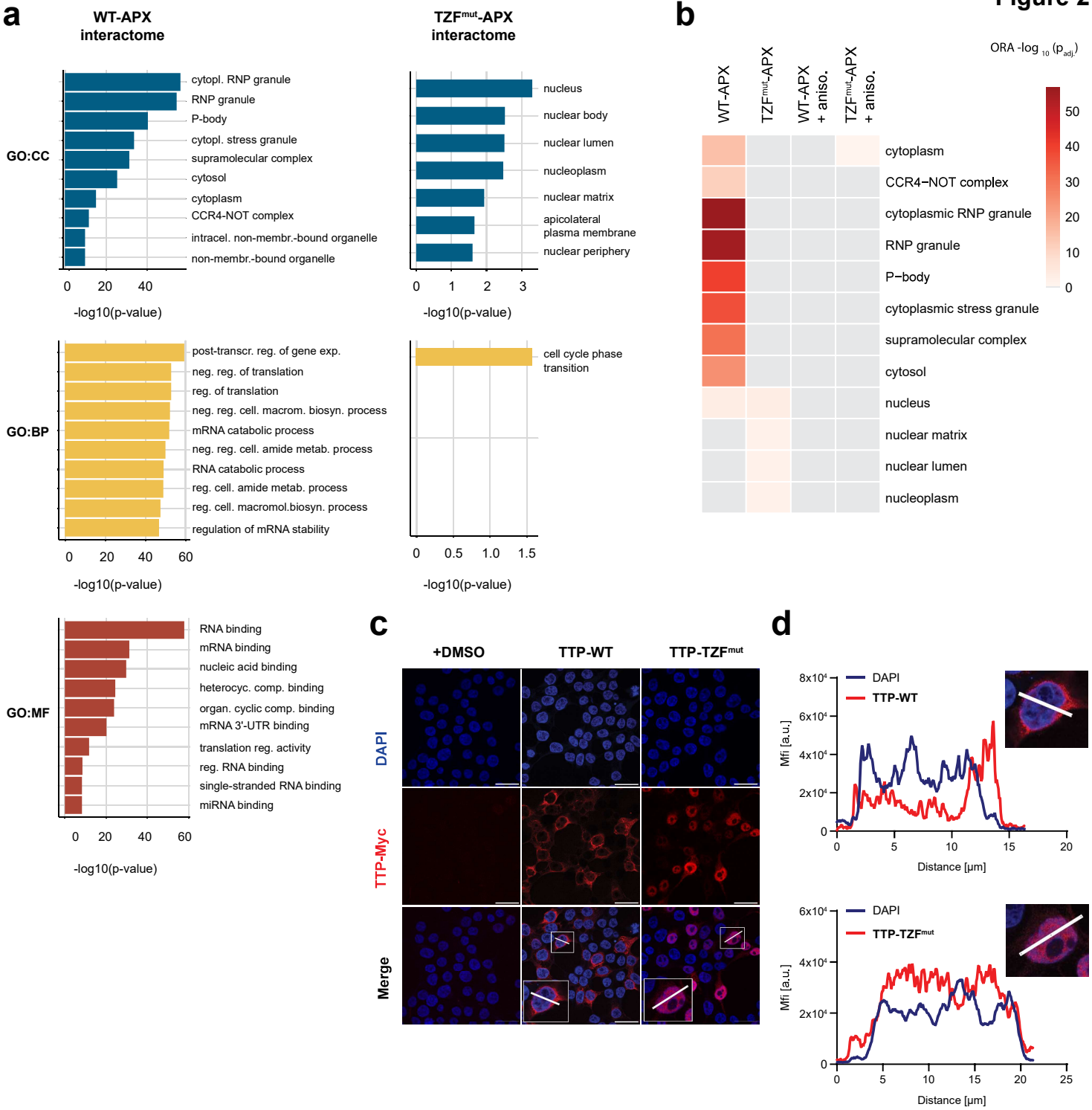
a
WT-APX interactome
TZFmut-APX interactome
GO:CC
cytopl. RNP granule
RNP granule
P-body
cytopl. stress granule
supramolecular complex
cytosol
cytoplasm
CCR4-NOT complex
intracel. non-membr.-bound organelle
non-membr.-bound organelle
nucleus
nuclear body
nuclear lumen
nucleoplasm
nuclear matrix
apicolateral plasma membrane
nuclear periphery
-log10(p-value)
GO:BP
post-transcr. reg. of gene exp.
neg. reg. of translation
reg. of translation
neg. reg. cell. macrom. biosyn. process
mRNA catabolic process
neg. reg. cell. amide metab. process
RNA catabolic process
reg. cell. amide metab. process
reg. cell. macromol.biosyn. process
regulation of mRNA stability
cell cycle phase transition
GO:MF
RNA binding
mRNA binding
nucleic acid binding
heterocyc. comp. binding
organ. cyclic comp. binding
mRNA 3'-UTR binding
translation reg. activity
reg. RNA binding
single-stranded RNA binding
miRNA binding
b
WT-APX
TZFmut-APX
WT-APX + aniso.
TZFmut-APX + aniso.
ORA -log10 (padj.)
cytoplasm
CCR4−NOT complex
cytoplasmic RNP granule
RNP granule
P−body
cytoplasmic stress granule
supramolecular complex
cytosol
nucleus
nuclear matrix
nuclear lumen
nucleoplasm
c
+DMSO
TTP-WT
TTP-TZFmut
DAPI
TTP-Myc
Merge
d
DAPI
TTP-WT
Mfi [a.u.]
Distance [µm]
TTP-TZFmut

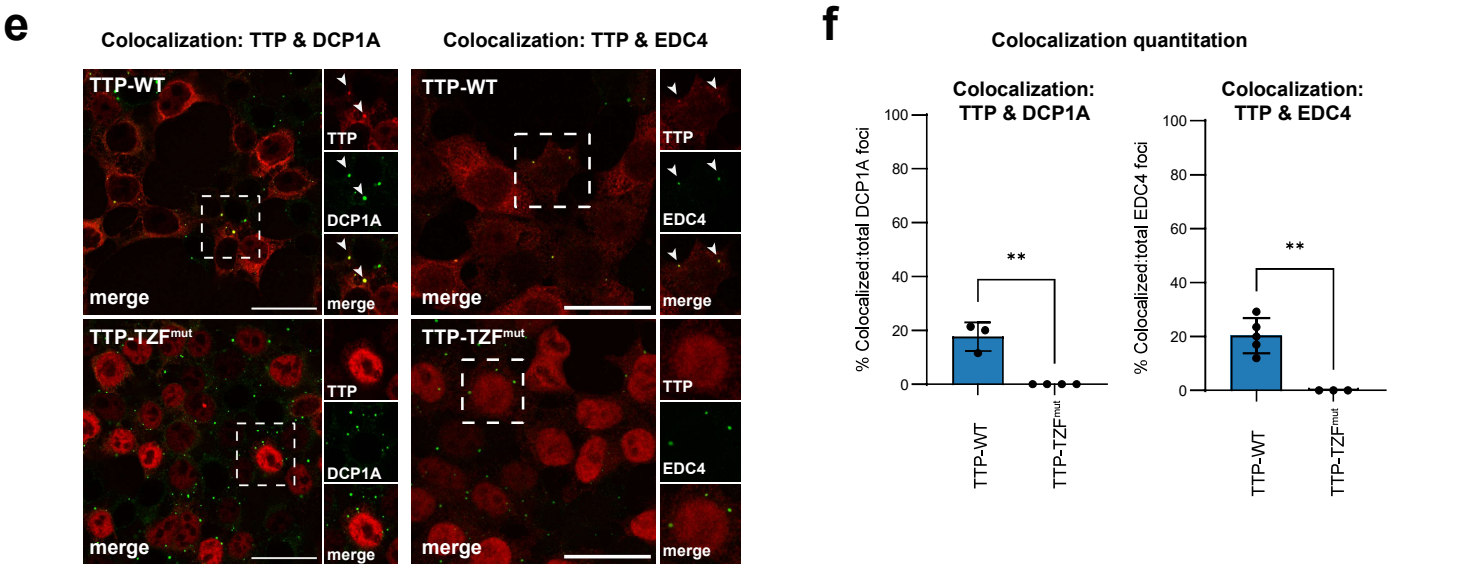
e
Colocalization: TTP & DCP1A
Colocalization: TTP & EDC4
TTP-WT
TTP-TZFmut
TTP
DCP1A
EDC4
merge
f
Colocalization quantitation
Colocalization: TTP & DCP1A
Colocalization: TTP & EDC4
% Colocalized:total DCP1A foci
% Colocalized:total EDC4 foci
**
TTP-WT
TTP-TZFmut

Figure 3

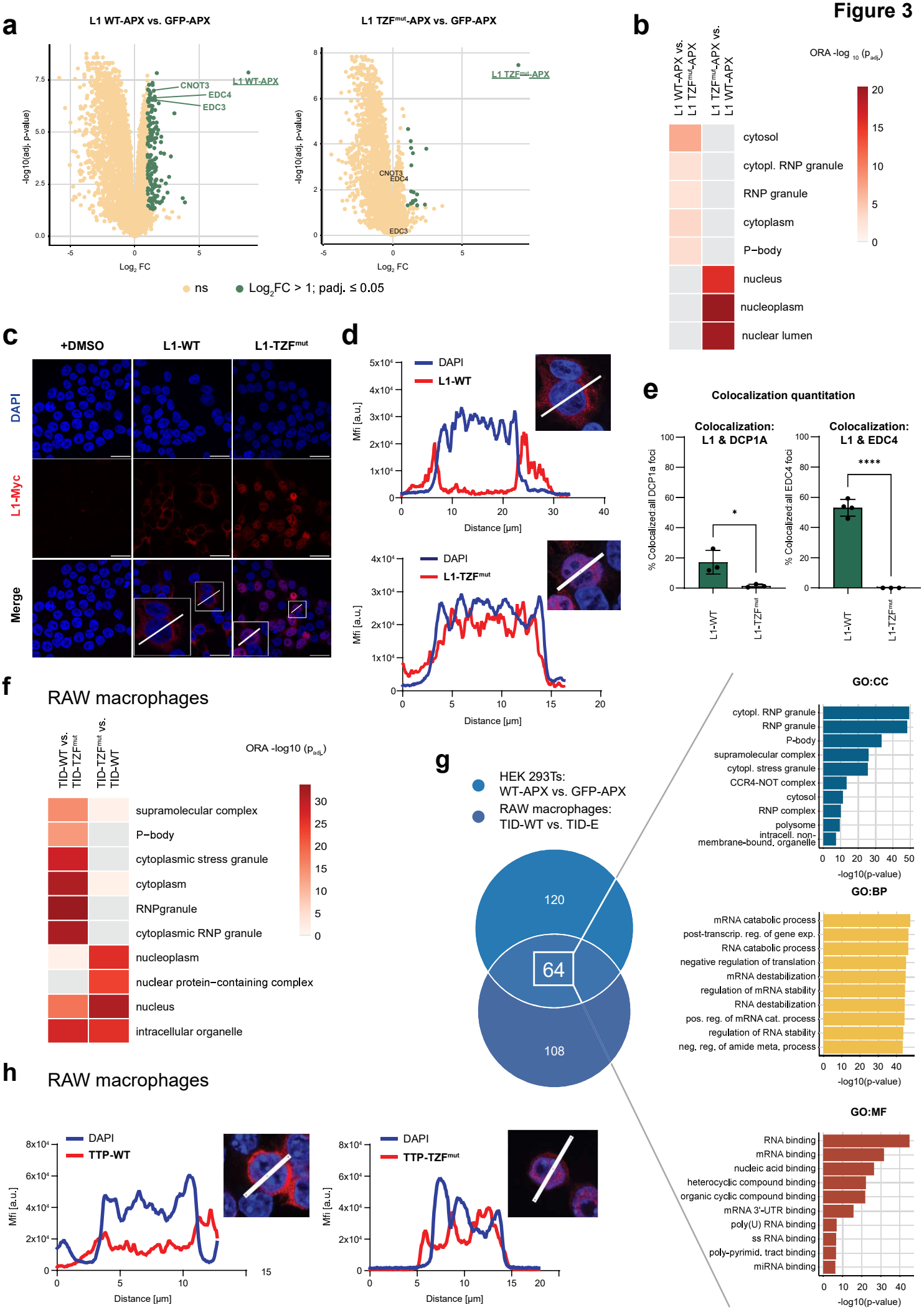
a
L1 WT-APX vs. GFP-APX
L1 TZFmut-APX vs. GFP-APX
CNOT3
EDC4
EDC3
L1 WT-APX
L1 TZFmut-APX
-log10(adj. p-value)
Log2 FC
ns
Log2FC > 1; padj. ≤ 0.05
b
L1 WT-APX vs. L1 TZFmut-APX
L1 TZFmut-APX vs. L1 WT-APX
ORA -log10 (padj.)
cytosol
cytopl. RNP granule
RNP granule
cytoplasm
P−body
nucleus
nucleoplasm
nuclear lumen
c
+DMSO
L1-WT
L1-TZFmut
DAPI
L1-Myc
Merge
d
DAPI
L1-WT
L1-TZFmut
Mfi [a.u.]
Distance [µm]
e
Colocalization quantitation
Colocalization: L1 & DCP1A
Colocalization: L1 & EDC4
% Colocalized:all DCP1a foci
% Colocalized:all EDC4 foci
L1-WT
L1-TZFmut
f
RAW macrophages
TID-WT vs. TID-TZFmut
TID-TZFmut vs. TID-WT
ORA -log10 (padj.)
supramolecular complex
P−body
cytoplasmic stress granule
cytoplasm
RNPgranule
cytoplasmic RNP granule
nucleoplasm
nuclear protein−containing complex
nucleus
intracellular organelle
g
HEK 293Ts: WT-APX vs. GFP-APX
RAW macrophages: TID-WT vs. TID-E
120
64
108
GO:CC
cytopl. RNP granule
RNP granule
P-body
supramolecular complex
cytopl. stress granule
CCR4-NOT complex
cytosol
RNP complex
polysome
intracell. non-membrane-bound. organelle
-log10(p-value)
GO:BP
mRNA catabolic process
post-transcrip. reg. of gene exp.
RNA catabolic process
negative regulation of translation
mRNA destabilization
regulation of mRNA stability
RNA destabilization
pos. reg. of mRNA cat. process
regulation of RNA stability
neg. reg. of amide meta. process
GO:MF
RNA binding
mRNA binding
nucleic acid binding
heterocyclic compound binding
organic cyclic compound binding
mRNA 3'-UTR binding
poly(U) RNA binding
ss RNA binding
poly-pyrimid. tract binding
miRNA binding
h
RAW macrophages
DAPI
TTP-WT
TTP-TZFmut
Mfi [a.u.]
Distance [µm]

Figure 4

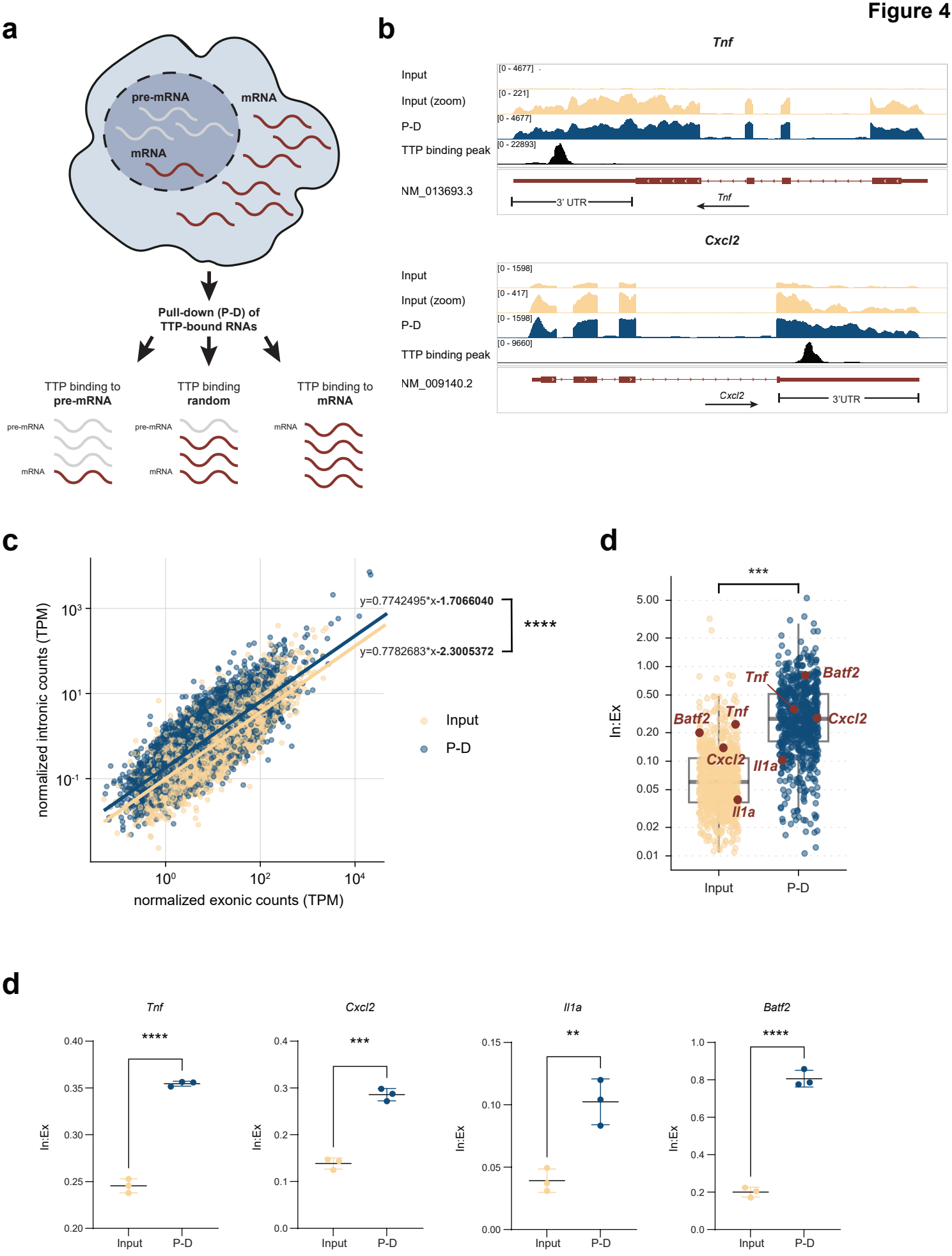
a
pre-mRNA
mRNA
mRNA
Pull-down (P-D) of TTP-bound RNAs
TTP binding to pre-mRNA
TTP binding random
TTP binding to mRNA
pre-mRNA
mRNA
b
Tnf
Input
Input (zoom)
P-D
TTP binding peak
NM_013693.3
[0 - 4677]
[0 - 221]
[0 - 22893]
3' UTR
Cxcl2
NM_009140.2
[0 - 1598]
[0 - 417]
[0 - 9660]
3'UTR
c
y=0.7742495*x-1.7066040
y=0.7782683*x-2.3005372
****
Input
P-D
normalized intronic counts (TPM)
normalized exonic counts (TPM)
d
***
Tnf
Batf2
Cxcl2
Il1a
In:Ex
Input
P-D
d
Tnf
Cxcl2
Il1a
Batf2
****
***
**
****
In:Ex
Input
P-D

Figure 5

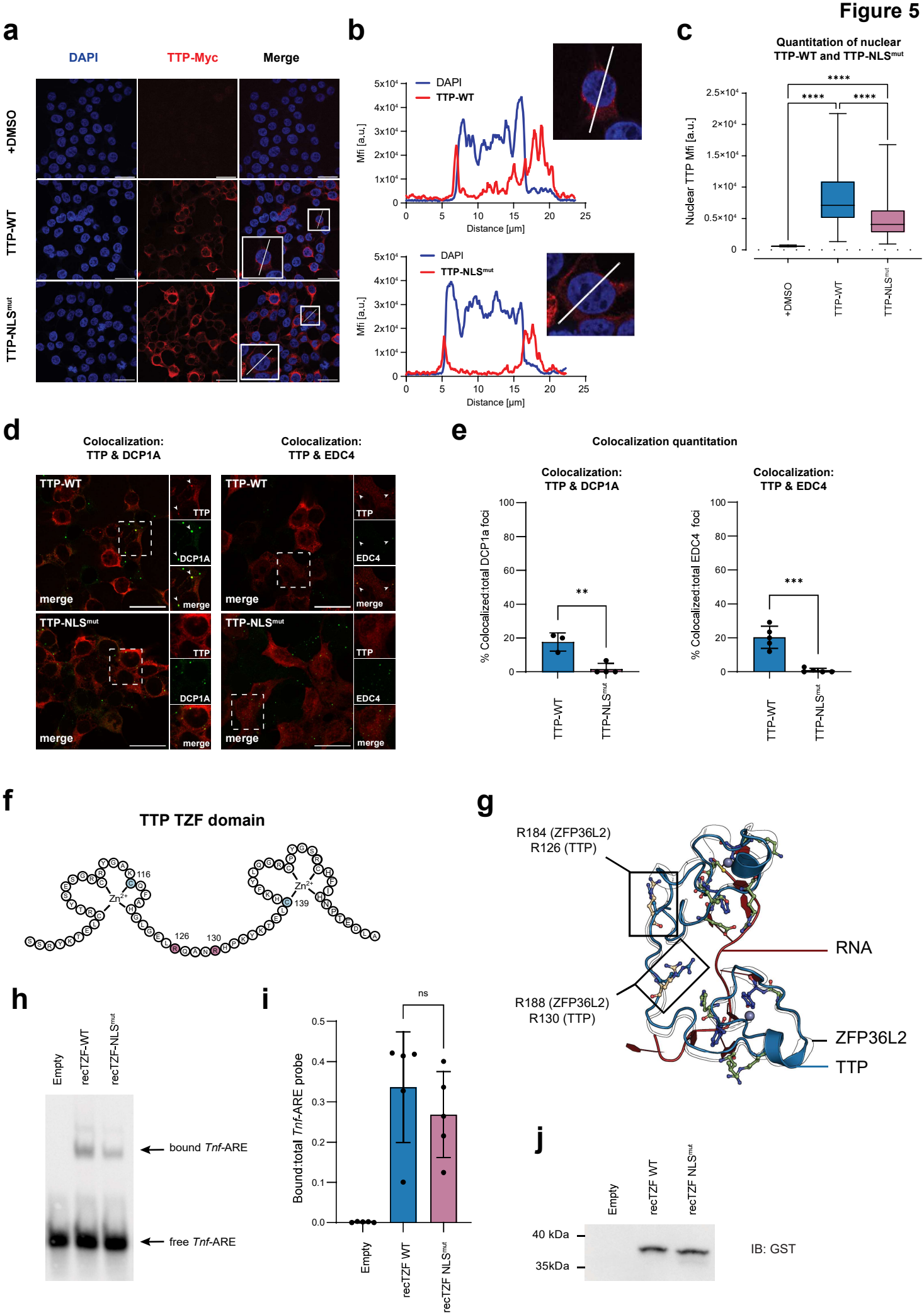
a
DAPI
TTP-Myc
Merge
+DMSO
TTP-WT
TTP-NLSmut
b
DAPI
TTP-WT
Mfi [a.u.]
Distance [µm]
DAPI
TTP-NLSmut
Mfi [a.u.]
Distance [µm]
c
Quantitation of nuclear TTP-WT and TTP-NLSmut
Nuclear TTP Mfi [a.u.]
****
****
****
+DMSO
TTP-WT
TTP-NLSmut
d
Colocalization: TTP & DCP1A
Colocalization: TTP & EDC4
TTP-WT
TTP
DCP1A
merge
EDC4
TTP-NLSmut
e
Colocalization quantitation
Colocalization: TTP & DCP1A
% Colocalized:total DCP1a foci
**
Colocalization: TTP & EDC4
% Colocalized:total EDC4 foci
***
TTP-WT
TTP-NLSmut
f
TTP TZF domain
116
126
130
139
g
R184 (ZFP36L2)
R126 (TTP)
RNA
R188 (ZFP36L2)
R130 (TTP)
ZFP36L2
TTP
h
Empty
recTZF-WT
recTZF-NLSmut
bound Tnf-ARE
free Tnf-ARE
i
ns
Bound:total Tnf-ARE probe
Empty
recTZF WT
recTZF NLSmut
j
Empty
recTZF WT
recTZF NLSmut
40 kDa
35kDa
IB: GST

Figure 6

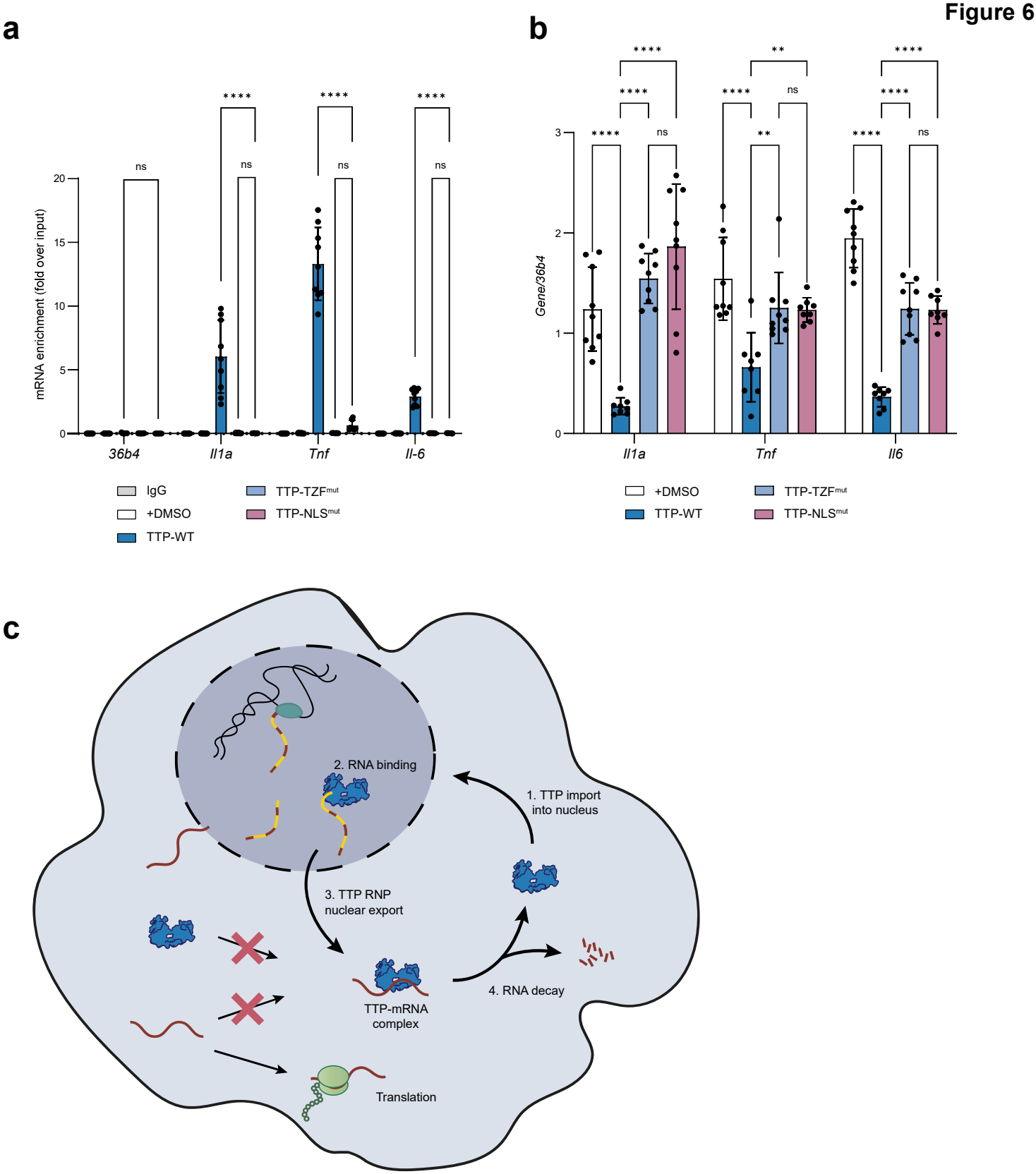
a
mRNA enrichment (fold over input)
20
15
10
5
0
ns
****
36b4
Il1a
Tnf
Il-6
IgG
+DMSO
TTP-WT
TTP-TZFmut
TTP-NLSmut
b
Gene/36b4
3
2
1
0
**
Il1a
Tnf
Il6
+DMSO
TTP-WT
TTP-TZFmut
TTP-NLSmut
c
2. RNA binding
1. TTP import
into nucleus
3. TTP RNP
nuclear export
TTP-mRNA
complex
4. RNA decay
Translation

Extended Data Fig.1

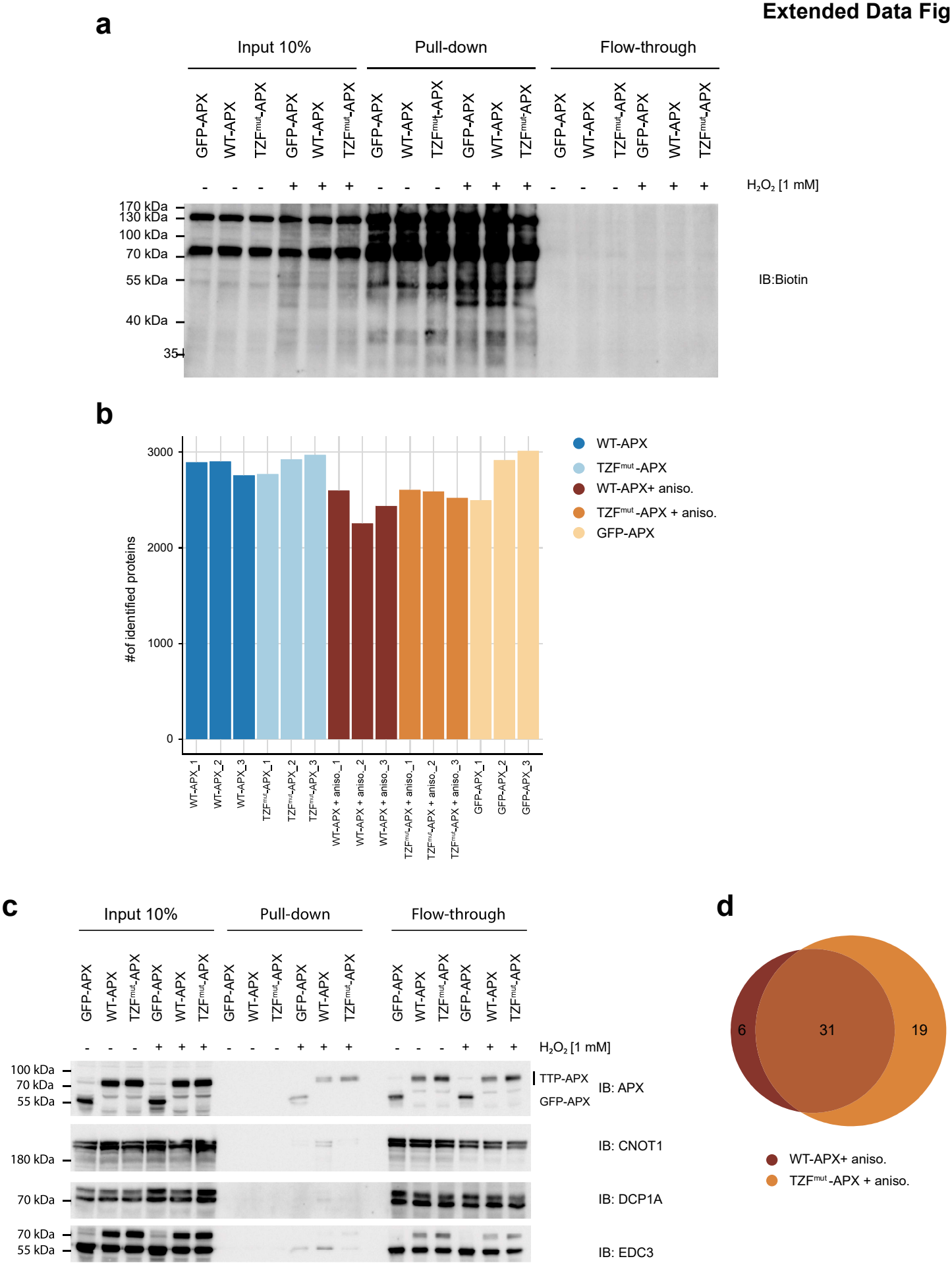

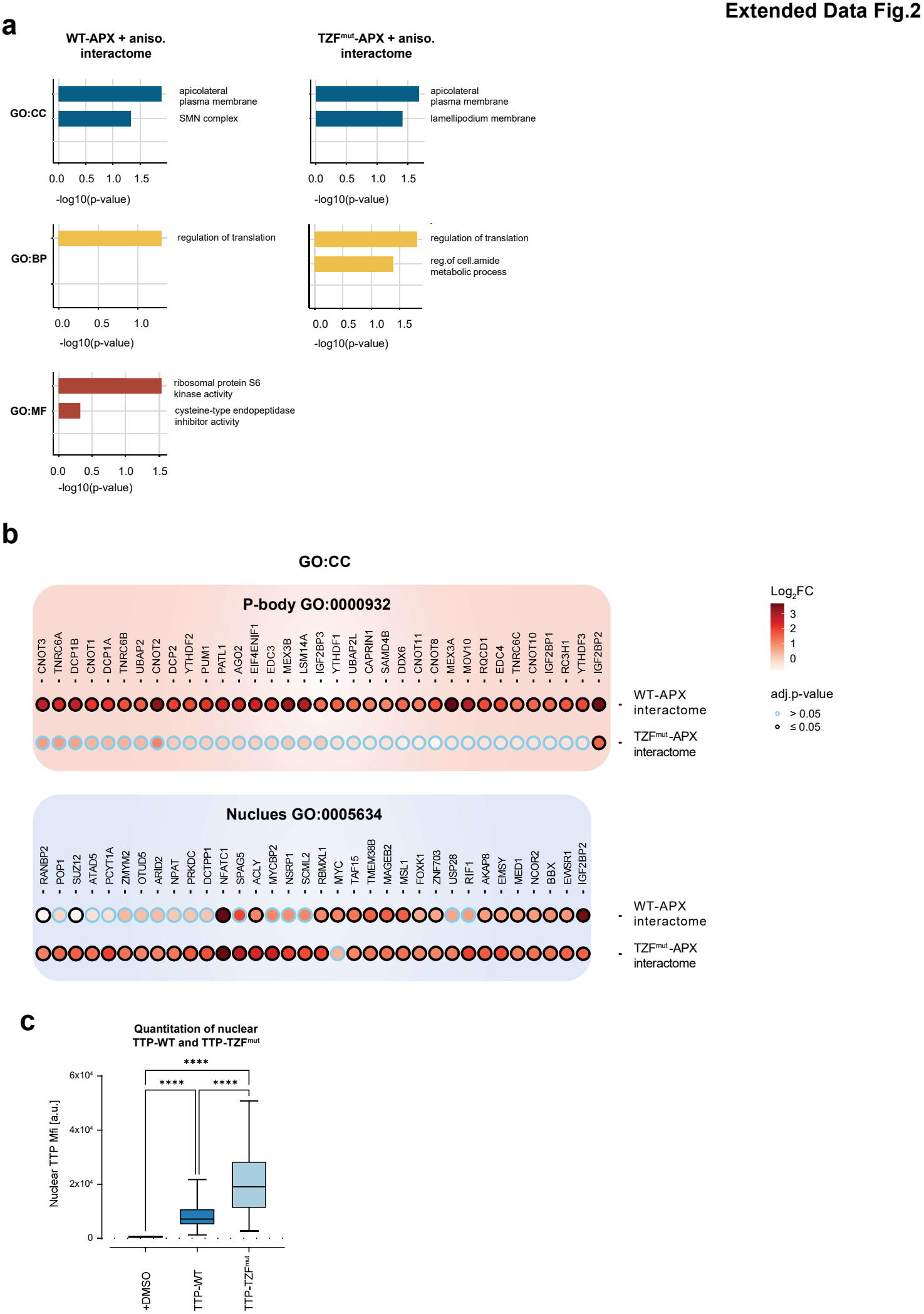
a
WT-APX + aniso. interactome
TZFmut-APX + aniso. interactome
GO:CC
apicolateral plasma membrane
SMN complex
lamellipodium membrane
GO:BP
regulation of translation
reg.of cell.amide metabolic process
GO:MF
ribosomal protein S6 kinase activity
cysteine-type endopeptidase inhibitor activity
-log10(p-value)
b
GO:CC
P-body GO:0000932
CNOT3 TNRC6A DCP1B CNOT1 DCP1A TNRC6B UBAP2 CNOT2 DCP2 YTHDF2 PUM1 PATL1 AGO2 EIF4ENIF1 EDC3 MEX3B LSM14A IGF2BP3 YTHDF1 UBAP2L CAPRIN1 SAMD4B DDX6 CNOT11 CNOT8 MEX3A MOV10 RQCD1 EDC4 TNRC6C CNOT10 IGF2BP1 RC3H1 YTHDF3 IGF2BP2
Nuclues GO:0005634
RANBP2 POP1 SUZ12 ATAD5 PCYT1A ZMYM2 OTUD5 ARID2 NPAT PRKDC DCTPP1 NFATC1 SPAG5 ACLY MYCBP2 NSRP1 SCML2 RBMXL1 MYC TAF15 TMEM38B MAGEB2 MSL1 FOXK1 ZNF703 USP28 RIF1 AKAP8 EMSY MED1 NCOR2 BBX EWSR1 IGF2BP2
WT-APX interactome
TZFmut-APX interactome
Log2FC
3
2
1
0
adj.p-value
> 0.05
≤ 0.05
c
Quantitation of nuclear TTP-WT and TTP-TZFmut
Nuclear TTP Mfi [a.u.]
6x10⁴
4x10⁴
2x10⁴
0
****
+DMSO
TTP-WT
TTP-TZFmut

Extended Data Fig.3

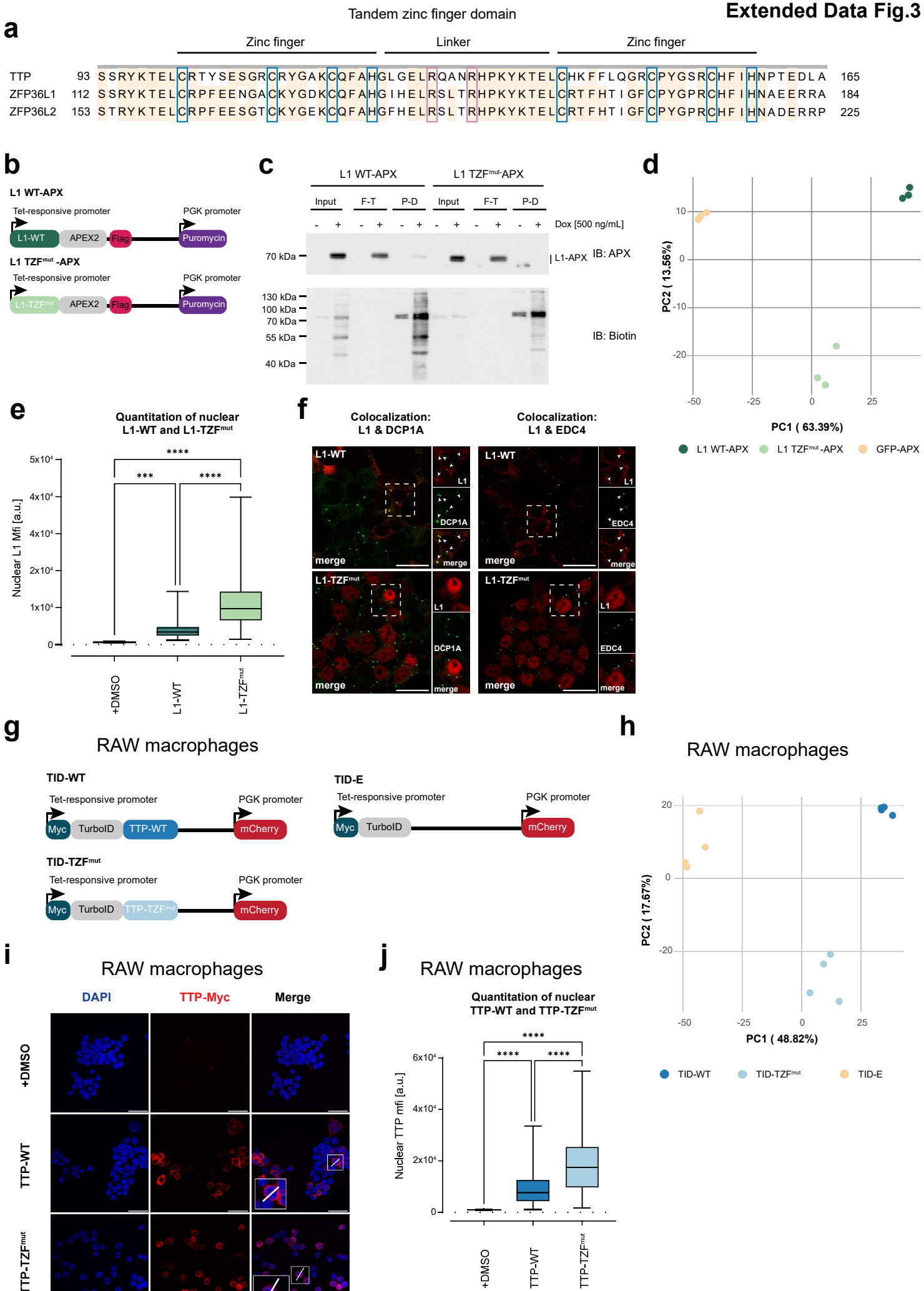

Extended Data Fig.4

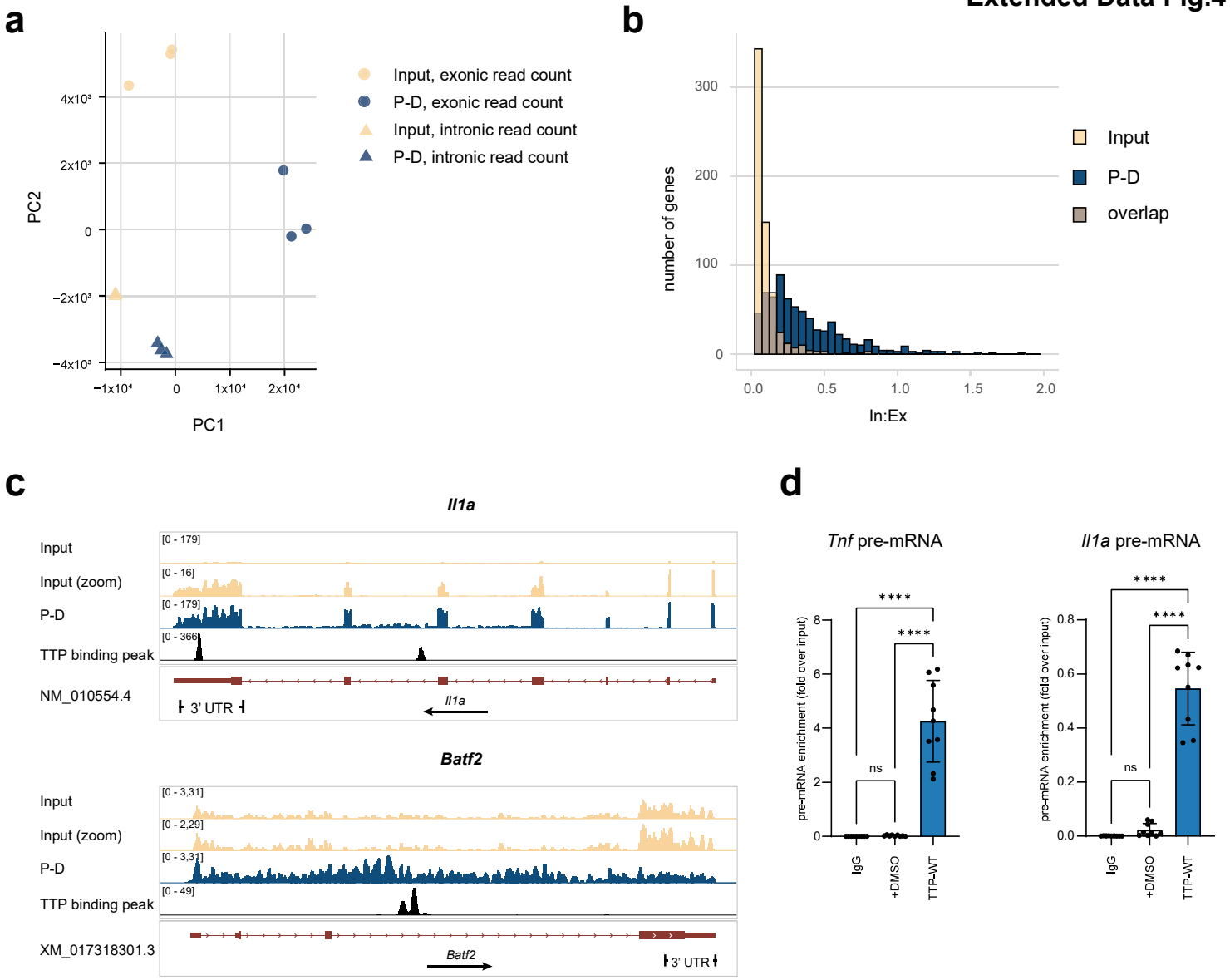

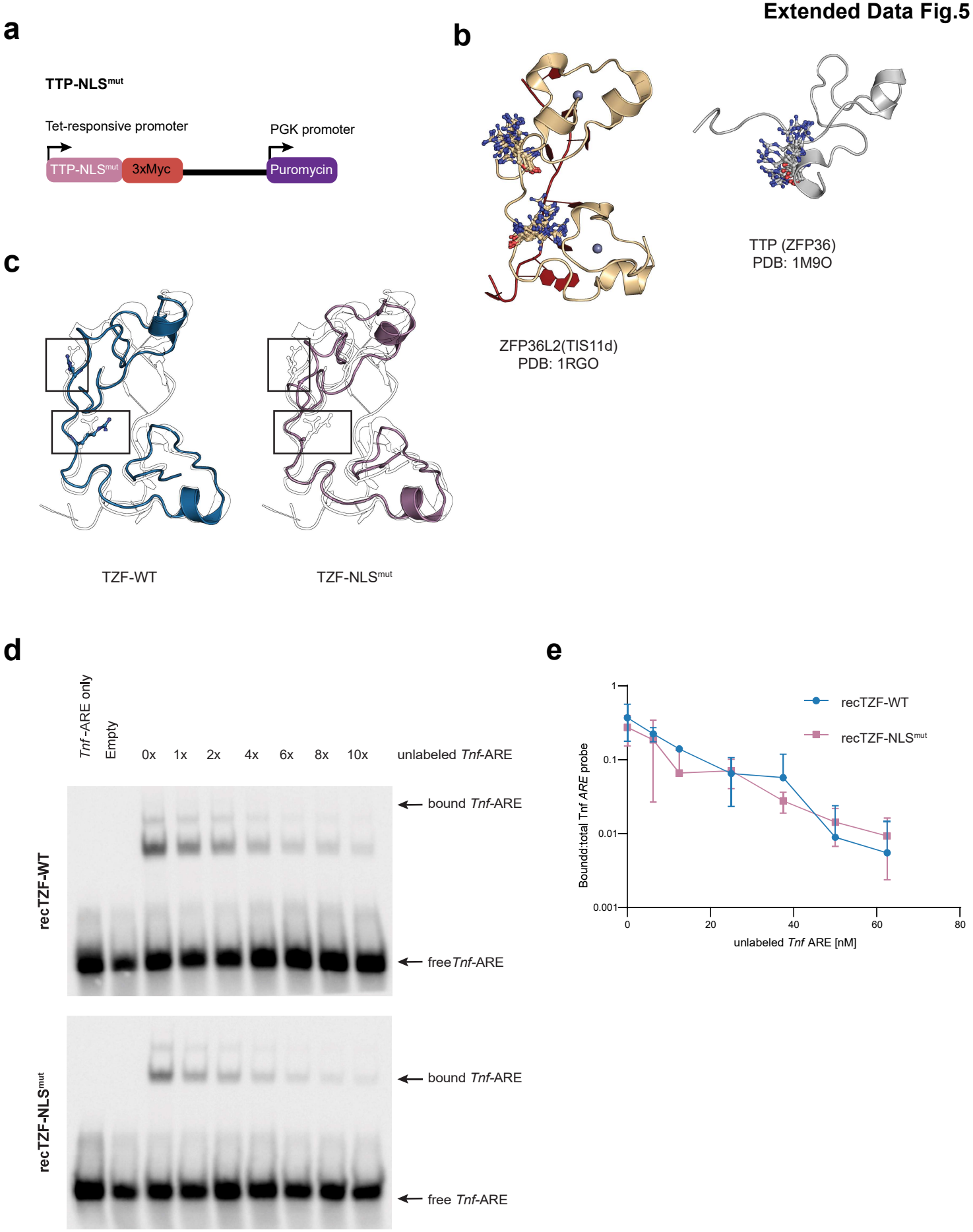
a
TTP-NLSmut
Tet-responsive promoter
PGK promoter
TTP-NLSmut
3xMyc
Puromycin
b
ZFP36L2(TIS11d)
PDB: 1RGO
TTP (ZFP36)
PDB: 1M9O
c
TZF-WT
TZF-NLSmut
d
Tnf-ARE only
Empty
0x
1x
2x
4x
6x
8x
10x
unlabeled Tnf-ARE
recTZF-WT
bound Tnf-ARE
free Tnf-ARE
recTZF-NLSmut
bound Tnf-ARE
free Tnf-ARE
e
recTZF-WT
recTZF-NLSmut
Boundd:total Tnf ARE probe
1
0.1
0.01
0.001
0
20
40
60
80
unlabeled Tnf ARE [nM]

a

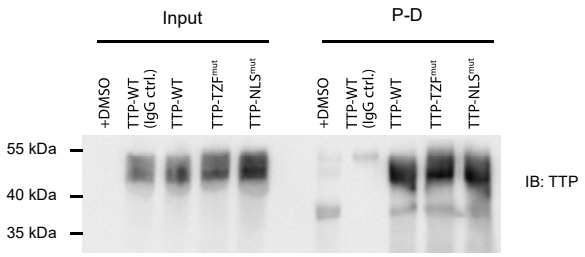
Input
P-D
+DMSO
TTP-WT (IgG ctrl.)
TTP-WT
TTP-TZF^{mut}
TTP-NLS^{mut}
+DMSO
TTP-WT (IgG ctrl.)
TTP-WT
TTP-TZF^{mut}
TTP-NLS^{mut}
55 kDa
40 kDa
35 kDa
IB: TTP